Nature and origin of the hematite-bearing plains of Terra Meridiani based on analyses of orbital and Mars Exploration rover data sets

R. E. Arvidson,[1] F. Poulet,[2] R. V. Morris,[3] J.-P. Bibring,[2] J. F. Bell III,[4] S. W. Squyres,[4] P. R. Christensen,[5] G. Bellucci,[6] B. Gondet,[2] B. L. Ehlmann,[7] W. H. Farrand,[8] R. L. Fergason,[5] M. Golombek,[9] J. L. Griffes,[1] J. Grotzinger,[10] E. A. Guinness,[1] K. E. Herkenhoff,[11] J. R. Johnson,[11] G. Klingelhöfer,[12] Y. Langevin,[2] D. Ming,[3] K. Seelos,[1] R. J. Sullivan,[4] J. G. Ward,[1] S. M. Wiseman,[1] and M. Wolff[8]

Received 7 April 2006; revised 10 July 2006; accepted 13 July 2006; published 22 November 2006.

[1] The ~5 km of traverses and observations completed by the Opportunity rover from Endurance crater to the Fruitbasket outcrop show that the Meridiani plains consist of sulfate-rich sedimentary rocks that are largely covered by poorly-sorted basaltic aeolian sands and a lag of granule-sized hematitic concretions. Orbital reflectance spectra obtained by Mars Express OMEGA over this region are dominated by pyroxene, plagioclase feldspar, crystalline hematite (i.e., concretions), and nano-phase iron oxide dust signatures, consistent with Pancam and Mini-TES observations. Mössbauer Spectrometer observations indicate more olivine than observed with the other instruments, consistent with preferential optical obscuration of olivine features in mixtures with pyroxene and dust. Orbital data covering bright plains located several kilometers to the south of the landing site expose a smaller areal abundance of hematite, more dust, and a larger areal extent of outcrop compared to plains proximal to the landing site. Low-albedo, low-thermal-inertia, windswept plains located several hundred kilometers to the south of the landing site are predicted from OMEGA data to have more hematite and fine-grained olivine grains exposed as compared to the landing site. Low calcium pyroxene dominates spectral signatures from the cratered highlands to the south of Opportunity. A regional-scale model is presented for the formation of the plains explored by Opportunity, based on a rising ground water table late in the Noachian Era that trapped and altered local materials and aeolian basaltic sands. Cessation of this aqueous process led to dominance of aeolian processes and formation of the current configuration of the plains.

Citation: Arvidson, R. E., et al. (2006), Nature and origin of the hematite-bearing plains of Terra Meridiani based on analyses of orbital and Mars Exploration rover data sets, *J. Geophys. Res.*, *111*, E12S08, doi:10.1029/2006JE002728.

1. Introduction

[2] The Mars Exploration rover, Opportunity, touched down on Meridiani Planum on 24 January 2004 and started an extensive campaign to explore the plains and craters in the vicinity of the landing site [*Squyres et al.*, 2004a]. At approximately the same time, the Mars Express Orbiter began observing Mars, including coverage of the Spirit and Opportunity landing sites with the Mars Express Observatoire pour la Minéralogie, l'Eau, les Glaces et l'Activité (OMEGA) hyperspectral imaging system (0.35 to 5.08 μm) [*Bibring et al.*, 2005]. In addition, the two orbiters Mars Global Surveyor (MGS) [*Albee et al.*, 2001] and Mars Odyssey [*Saunders et al.*, 2004] continued to observe Mars. The purpose of this paper is to report results from examination and analyses of orbital data along with data from the Athena Payload on Opportunity [*Squyres et al.*, 2003], focusing on the nature and origin of soils and outcrops at Meridiani Planum. Specific emphasis is placed on analyses

[1]Department of Earth and Planetary Sciences, Washington University, St. Louis, Missouri, USA.
[2]Institut d'Astrophysique Spatiale, Université Paris-Sud, Orsay, France.
[3]NASA Johnson Space Center, Houston, Texas, USA.
[4]Department of Astronomy, Cornell University, Ithaca, New York, USA.
[5]Department of Geological Sciences, Arizona State University, Tempe, Arizona, USA.
[6]Istituto di Fisica dello Spazio Interplanetario, Istituto Nazionale di Astrofisica, Rome, Italy.
[7]School of Geography and Environment, University of Oxford, Oxford, UK.
[8]Space Science Institute, Boulder, Colorado, USA.
[9]Jet Propulsion Laboratory, Pasadena, California, USA.
[10]Geological and Planetary Sciences, California Institute of Technology, Pasadena, California, USA.
[11]U.S. Geological Survey, Flagstaff, Arizona, USA.
[12]Institut für Anorganische und Analytische Chemie, Johannes Gutenberg-Universität, Mainz, Germany.

0148-0227/06/2006JE002728

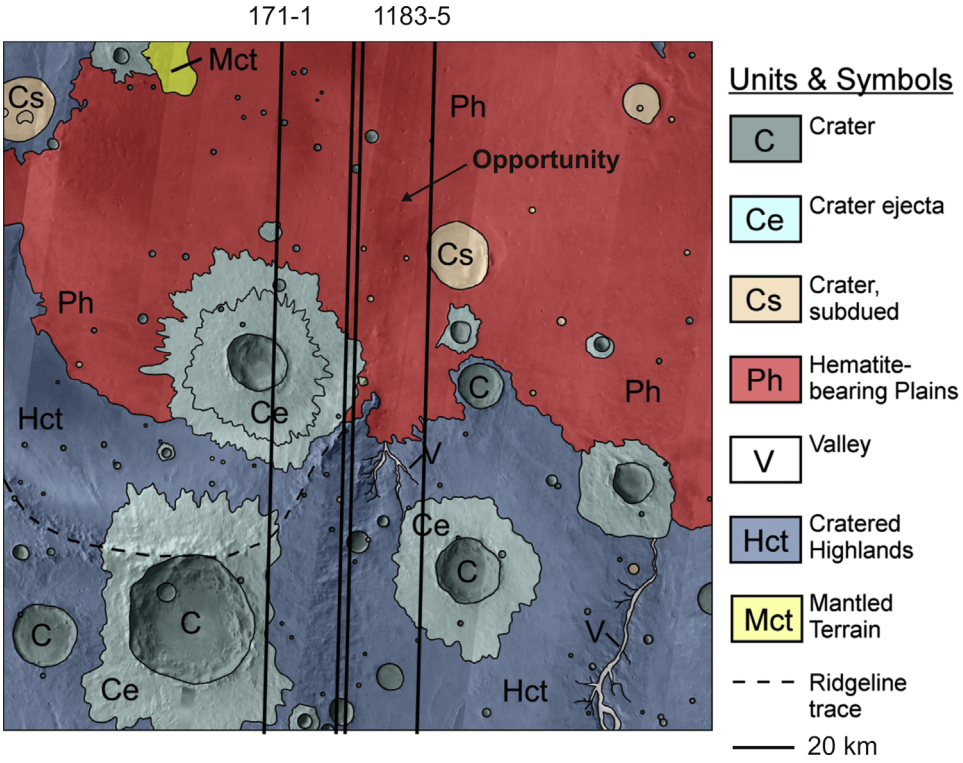

Figure 1. Geologic map of the Opportunity landing site and surrounding areas superimposed on a mosaic compiled from THEMIS daytime IR images. Footprints for OMEGA coverage for orbits 171-1 and 1183-5 are also shown. The oldest units are the cratered highlands (Hct). Hematite-bearing plains (Ph) sit unconformably on the cratered highlands. Etched terrain materials beneath the Ph units and discussed in the text are not exposed in the mapped area. Note channel systems buried by Ph materials, the crater with its ejecta deposit overlying the Ph unit and covered by data for orbit 171-1, and partially buried crater to southeast of Opportunity and labeled CS. Image is a Mars Equirectangular map projection.

of OMEGA data and implications for the presence and abundances of minerals that are exposed on the plains.

[3] The first part of this paper provides a regional-scale overview of the geomorphology, stratigraphy, and ages of units exposed in Terra Meridiani, including the hematite-bearing plains of Meridiani Planum. The overview takes advantage of published work as well as analyses presented in this paper using Mars Odyssey Thermal Emission Imaging System (THEMIS) [*Christensen et al.*, 2004a] and MGS Mars Orbiter Camera (MOC) [*Malin et al.*, 1992] data. OMEGA hyperspectral reflectance data covering the plains (including the landing site) and the cratered terrains to the south of the plains are placed in this regional context. The extensive Panoramic Camera (Pancam) [*Bell et al.*, 2003], Miniature Thermal Emission Spectrometer (Mini-TES) [*Christensen et al.*, 2003], Navigation Camera (Navcam) [*Maki et al.*, 2003], Hazard Avoidance Camera (Hazcam) [*Maki et al.*, 2003], Microscopic Imager (MI) [*Herkenhoff et al.*, 2003], Alpha Particle X-Ray Spectrometer (APXS) [*Rieder et al.*, 2003], and Mössbauer (MB) [*Klingelhöfer et al.*, 2003] data acquired by Opportunity along its ~5 km of traverses from the landing site to the Fruitbasket outcrop (sols 1 to ~560; see S. W. Squyres et al. (Overview of the Opportunity Mars Exploration rover mission to Meridiani Planum: Eagle crater to Purgatory ripple, submitted to *Journal of Geophysical Research*, 2006) (hereinafter referred to as Squyres et al., submitted manuscript, 2006) for an overview of mission operations during this time period) are then used as "ground truth" to compare to the mineral abundances and grain sizes retrieved from OMEGA data for specific pixels covering the traverses. Similarities and differences are highlighted and discussed. Finally, a synthesis is presented that shows how the plains formed and evolved to the present distribution of deposits and landforms.

2. Regional-Scale Geologic Context

[4] The hematite-bearing plains of Meridiani Planum were identified and mapped from MGS Thermal Emission Spectrometer (TES) data based on comparisons with laboratory spectra of crystalline hematite [*Christensen et al.*, 2000, 2001] (Figure 1). Hematite was inferred to cover ~15% of the surface. Opportunity confirmed the surface coverage and discovered that the hematite signature is associated with ~1- to 5-mm-diameter concretions that have concentrated as an aeolian lag deposit weathered from sulfate-rich outcrops [*Christensen et al.*, 2004b; *Squyres et al.*, 2004b]. Other minerals present on the plains as inferred from TES observations include feldspar, pyroxene, and weathering products [*Arvidson et al.*, 2003].

[5] From orbit the hematite-bearing plains exhibit variable spatial patterns, ranging from bland, low-albedo surfaces (~0.15 Lambert albedo) interspersed with bright patches, to low-albedo dune fields [*Arvidson et al.*, 2003;

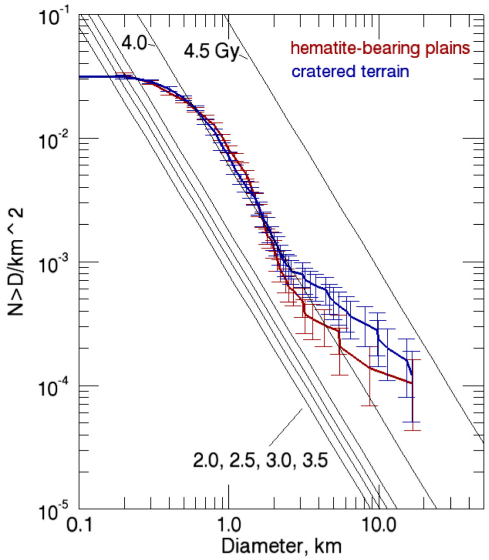

Figure 2. Cumulative crater size frequency distributions are shown for the cratered highlands and hematite-bearing plains, using the mosaic shown in Figure 1 as the base map for counts. The Hartmann production function and isochrons as defined by *Hartmann and Neukum* [2001] are also shown. Errors are the square root of the cumulative number of craters greater than a given size per square kilometer.

Christensen and Ruff, 2004]. Detailed mapping of the hematite-bearing plains and surrounding regions shows that these plains are at the top of a section of layered material that is probably hundreds of meters thick beneath the Opportunity landing site [*Hynek et al.*, 2002; *Arvidson et al.*, 2003; *Edgett*, 2005] (also J. L. Griffes et al., Geomorphic and spectral mapping of northern Meridiani Planum, submitted to *Journal of Geophysical Research*, 2006) (hereinafter referred to as Griffes et al., submitted manuscript, 2006) (Figure 1). A unit termed the etched terrain by *Hynek et al.* [2002] outcrops several hundred kilometers to the west, north, and east of the landing site as the hematite-bearing plains unit thins and the etched terrain materials are exposed. OMEGA data covering the etched terrains show enhanced water bands at ~1.9 and ~3.0 micrometers (F. Poulet et al., manuscript in preparation, 2006) and, in some localities, evidence for the presence of kieserite ($MgSO_4 \cdot H_2O$) and polyhydrated magnesium sulfate minerals where discrete stratigraphic horizons are exposed [*Gendrin et al.*, 2005; *Arvidson et al.*, 2005; Griffes et al., submitted manuscript, 2006].

[6] The etched terrain materials sit unconformably on the Noachian cratered terrain materials in some places, and in others may be part of the cratered terrain section [e.g., *Hynek et al.*, 2002; *Arvidson et al.*, 2003; *Edgett*, 2005]. Several hundred kilometers to the south of the landing site the cratered terrain exhibits channel systems that disappear beneath or merge into the hematite-bearing plains, implying an age for the plains materials in this locality that is younger than and in place contemporaneous with the channeling events (Figure 1). This inference is confirmed by examination of crater size frequency distributions derived from the cratered terrain and plains units (Figure 2). Specifically, the size frequency distributions for the hematite-bearing plains and cratered terrain overlap for sizes smaller than ~2 km across. This size range corresponds to a population of fresh-looking impact craters on the cratered terrain (i.e., formed after or during waning stage of fluvial erosion) and to craters clearly superimposed on the plains materials. Larger craters for both units show a complex size distribution associated with either the impactor size distribution and/or a period of crater erosion and burial that preferentially removed smaller craters before the population of fresh craters began forming and being retained [e.g., *Chapman and Jones*, 1977; *Neukum and Ivanov*, 1996]. The craters in the cratered terrain in this larger size range appear degraded, consistent with an early period of erosion and burial. On the plains, these larger craters appear to have been partially buried by the plains deposits, including the ~20-km-diameter crater located ~20 km to the south-southeast of the Opportunity landing site (CS in Figure 1). Fitting the *Hartmann and Neukum* [2001] flux model to the data shows that the craters with diameters less than ~2 km across exhibit an age of ~4 Gy, although we note that the crater flux and thus the absolute timescale are only poorly known. The crater abundances do imply that the two surfaces began to preserve craters at the end of the Noachian to early Hesperian Eras; that is, fluvial erosion was finished, along with deposition of the Meridiani plains-forming materials. Implications of these results will be examined in detail in the discussion section of this paper.

3. Detailed Analyses of OMEGA, MOC, and THEMIS Data

3.1. OMEGA Data

[7] Several OMEGA passes cover the Opportunity landing site and surrounding plains. Data from two of the highest spatial resolution passes are discussed in this paper: orbits 171-1 (i.e., orbit 171, scene 1) and 1183-5 (Table 1). Orbit 171-1 is centered to the west of the landing site and covers the hematite-bearing plains, ejecta deposits from the

Table 1. Lighting and Viewing Geometries Associated With OMEGA and Pancam Spectral Data Shown in Paper[a]

Data Set	Date and Time	Incidence Angle, deg	Emission Angle, deg	Phase Angle, deg
OMEGA 1183-5: landing site	12/20/04; 14:00 LTST	33	18	32
OMEGA 171-1: west of landing site	3/4/04; 12:03 LTST	25	17	26
Pancam Sol 319: crossing tracks	12/16/04; 12:27 LMST	22	30	40
Pancam 367: Sol 366 trench	2/3/05; 12:54 LMST	19	25	22
Pancam 373: Sol 366 trench	2/9/05; 16:05 LMST	63	28	70
Pancam 511: Purgatory tracks	7/2/05; 12:11 LMST	20	48	67
Pancam 556: Fruitbasket outcrop	8/17/05; 11:51 LMST	23	17	41

[a]Pancam data used to extract Pancam spectra; only Pancam images from sol 319 are shown as a color figure. Dates given as month/day/year. LTST, local true solar time; LMST, local mean solar time.

~20-km crater to the southwest of the Opportunity site that excavated into and beneath plains materials, and cratered terrain to the south (Figure 1). Orbit 1183-5 goes directly over the Opportunity site and cratered terrain highlands to the south (Figure 1). Both data sets have 32 pixels across track and thousands of pixels along track (roughly aligned in a north-south direction), with pixel sizes of ~700 m along track and ~500 m cross track. The data sets consist of observations collected by the three components of the instrument: a push-broom spectrometer operating from 0.35 to 1.08 μm with 96 bands and 20 nm full width at half maximum intensity (FWHM), an infrared whisk-broom C spectrometer, operating from 0.98 to 2.6 μm with 128 bands and 20 nm FWHM, and an infrared whisk-broom L spectrometer, operating from 2.5 to 5.08 μm with 128 bands and 30 nm FWHM [*Bibring et al.*, 2005]. The three spectrometers have different fields of view. Use of the longest wavelength portion of the L spectrometer has been problematic because of radiance calibration issues and the complex interplay of reflected solar radiation and surface emission that is characteristic of this part of the spectrum. In this paper we present data from the 0.35 to 4.0 μm wavelength region and focus on quantitative analyses of the well-calibrated C spectrometer data.

3.2. I/F Spectra

[8] The first step in reduction of OMEGA data for any given band is calibration to I/F, where I is the scene radiance on sensor and F is the solar irradiance divided by π. The radiance values include both atmospheric and surface contributions. The calibration to units of I is based on preflight laboratory measurements combined with in-flight observations. The I/F values for the short wavelength and C spectrometers for OMEGA 1183-5 are shown in Figure 3 for an average of pixels (three rows (~500 m/pixel) by five columns (~700 m/pixel)) for the Opportunity landing site and terrains traversed from Eagle crater to the Fruitbasket outcrop located ~3 km south of Endurance crater (Squyres et al., submitted manuscript, 2006). To better understand the contributions from atmospheric gases, dust, and ice aerosols, the data for OMEGA 1183-5 over the Opportunity site were also modeled with the DISORT radiative modeling code [*Stamnes et al.*, 1988] (Figure 3). The code models gas absorptions (CO_2, CO, H_2O), and scattering and absorption resulting from dust and ice aerosols, along with surface and atmospheric emission. The inputs for the code included an atmospheric pressure and temperature profile, aerosol dust and ice optical depths for the time and location of the observation, observation and viewing geometries appropriate for the observations, nominal passband centers and FWHM for the three OMEGA spectrometers, and input surface reflectances. A surface temperature of 284 K based on Mini-TES observations and climatological optical depths of dust = 0.35 and ice = 0.05 at reference wavelengths of 9.3 and 12.1 microns, respectively, were used in the modeling [*Smith*, 2004]. The input surface reflectances were modeled as spectrally flat input Lambert Albedos. Five model spectra were calculated and shown in Figure 3. Calculating the single scattering albedo and scaling the optical depths to the OMEGA wavelengths were done using the particle size distribution (for dust nominal loading) and indices of refraction from *Wolff and Clancy* [2003], which incorporates laboratory measurements of dehydrated palagonite in the near-infrared. The aerosol scattering phase function was adopted from *Clancy et al.* [2003]. The equation of state was determined by a Runge-Kutte integration of the equation of hydrostatic equilibrium, using MOLA-derived aeroid and Mini-TES (plus TES) temperature data [e.g., *Smith et al.*, 2004]. Molecular absorption parameters were calculated using the correlated-k approach with HITRAN line parameters.

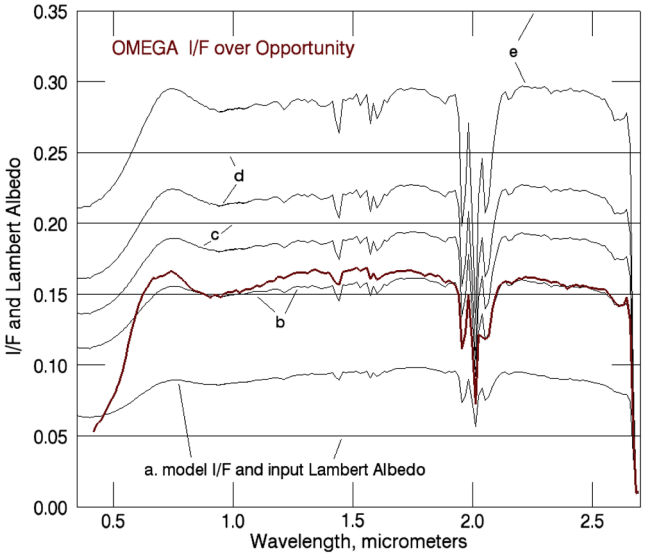

Figure 3. Series of spectra illustrating theoretical I/F values that would be observed by the OMEGA instrument VNIR and C spectrometers for orbit 1183-5, together with model gray surface Lambert Albedos (a = 0.05, b = 0.15, c = 0.20, d = 0.25, and e = 0.35) used to compute the I/F values. Effects of atmospheric gases and dust and ice aerosols were included in calculating I/F values. The red spectrum is an I/F spectrum for OMEGA 1183-5 data for pixels covering regions traversed by Opportunity. Note that model dark surfaces look brighter in I/F, whereas bright surfaces look darker as compared to Lambert albedo inputs. Further, atmospheric dust produces red I/F values for gray surfaces. CO_2 gas absorption bands are evident longward of ~1.3 μm. Note that the input 0.15 Lambert Albedo surface has apparent I/F values that are approximately equal to the Lambert Albedos for the ~1- to 2.5-μm wavelength range. The Opportunity site corresponds approximately to this input albedo, with a surface that is distinctly red at short wavelengths and has a slight rise that peaks at ~1.5 μm.

[9] Examination of the DISORT model output for the short wavelength and C spectrometer spectral ranges shows that spectrally gray surface albedos produce a red colored I/F spectrum in the visible to reflected infrared (to ~0.75 μm) and an absorption band at ~0.9 μm (Figure 3). This results from the presence of red dust in the atmosphere, where as noted the dust is based on the optical properties of fine-grained, very dry palagonite. The model spectra also clearly show the dominance of the CO_2 gas bands from ~1.4 to 2.6 μm. H_2O bands have minor impact on the spectra because of low H_2O concentrations (12 precipitable μm for model curves) in the typical Martian atmosphere. Note that the C spectrometer wavelengths are not highly influenced by

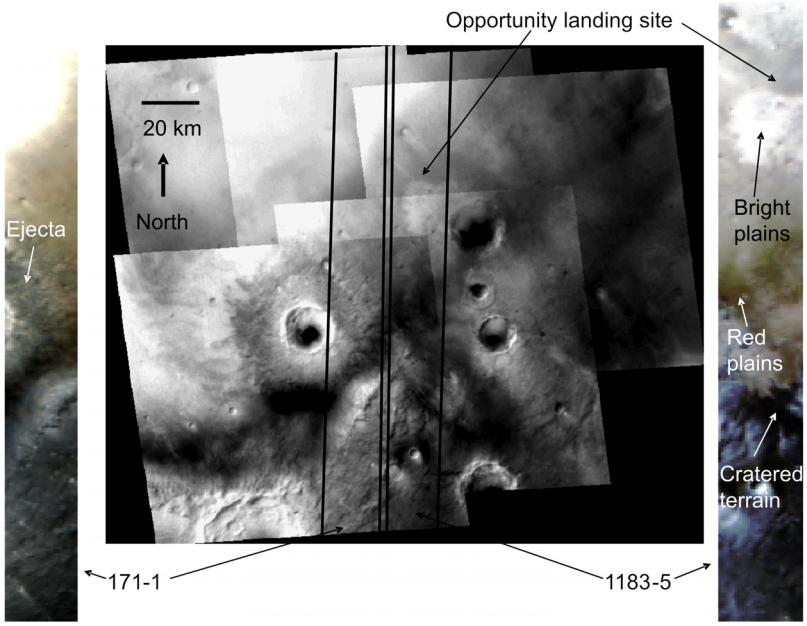

Figure 4. MOC Wide Angle camera image mosaic of Opportunity landing site and surroundings is shown together with OMEGA false color infrared images, using band assignments of 1.14, 1.50, and 2.27 μm as blue, green, and red colors, respectively. End member spectral locations for spectra shown in Figure 6 are labeled on the OMEGA images, with the exception of OMEGA 171-1 data. Note the dark aeolian splotches on the crater floors that indicate winds from the north to northwest and bright streaks indicative of winds from the northwest. Note also the dark albedo pattern that extends along the southern boundary of the hematite bearing plains and is nestled against the southern and southeastern rim of the large crater to the south of the Meridiani plains materials. The southeasterly extension of these dark materials occurs in a topographic low starting in the middle of the MOC image mosaic. Footprints for OMEGA orbits 171-1 and 1183-5 are shown. Image is a Mars Equirectangular projection.

the presence of aerosols and are only affected by gas band absorptions in particular wavelength intervals. These results also held for model runs in which the aerosol properties (optical depth and particle size distributions) were varied within reasonable limits. Also note that model low-albedo surfaces show I/F values that are higher than the input values, whereas intrinsically bright surfaces show I/F values that are darker than the input values. This is a consequence of the dominance of scattered skylight for the darker surfaces and attenuation of the radiance from the surface by the atmosphere for brighter surfaces.

[10] The OMEGA spectrum for the Opportunity landing site shows a surface that is distinctly red in the visible to infrared as compared to the model crystalline albedos, consistent with the presence of ferric oxides on the surface. This inference is confirmed by Pancam and MB measurements from Opportunity [*Bell et al.*, 2004; *Klingelhöfer et al.*, 2004]. The OMEGA spectrum for the Opportunity site also shows a subtle, broad reflectivity maximum near 1.5 μm relative to model crystalline albedos. The overall pattern is consistent with a surface spectrum that has subtle, broad absorptions at $\sim$1 and $\sim$2 μm, consistent with the presence of pyroxenes. This inference is supported by surface measurements from Opportunity [*Bell et al.*, 2004; *Christensen et al.*, 2004b; *Klingelhöfer et al.*, 2004]. No obvious features are present between 2.1 and 2.5 μm, where OMEGA data for etched terrains to the north and northeast of the landing site show the presence of water-related combination bands resulting from kieserite-like materials and polyhydrated sulfates [*Gendrin et al.*, 2005; *Arvidson et al.*, 2005; Griffes et al., submitted manuscript, 2006]. Rather, the 0.4- to 2.5-μm spectrum for the Opportunity site is controlled by the broadly varying features associated with charge transfer and electronic transition features.

3.3. OMEGA-Based I/F False Color IR Images and Relationships to MOC and THEMIS Data

[11] To facilitate visual analyses of the OMEGA C spectrometer data sets, false color IR composites were generated for the I/F values from OMEGA 1183-5 and 171-1 data using wavelengths of 1.14, 1.50, and 2.27 μm as blue, green, and red colors, respectively (Figures 3–5). The band selection was chosen on the basis of extensive examination of the C spectrometer data set, with the conclusion that selecting a wide wavelength range outside of regions with gas band absorptions provided an optimum presentation of the distribution of false color IR spatial patterns without a significant impact from aerosols.

[12] To facilitate interpretation of OMEGA false color IR trends a regional-scale MOC Wide Angle (WA) red band mosaic was generated (Figure 4), together with a thermal inertia (TI) map from THEMIS data (see *Fergason et al.* [2006] and Appendix A for data processing details) and a high-resolution MOC Narrow Angle image (calibrated to I/F) selected over the landing site and surroundings (Figure 5). All data sets were coregistered to a THEMIS VIS image

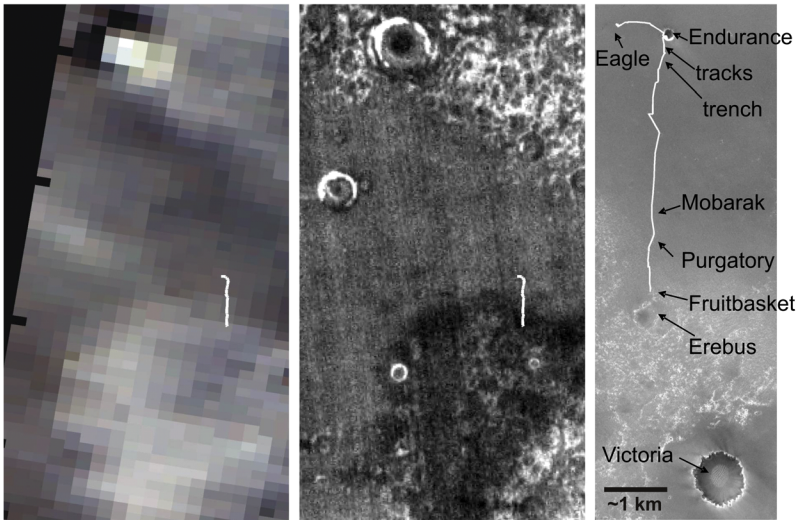

Figure 5. OMEGA false color IR composite from orbit 1183-5 (using band assignments of 1.14, 1.50, and 2.27 μm as blue, green, and red colors, respectively), THEMIS-based Thermal inertia (TI) map, and MOC NA frame of the Opportunity landing area are shown. Opportunity's traverses are plotted as white traces. Crater informal names and sols associated with various locations along Opportunity's traverses are shown on the MOC image. Victoria crater is approximately 750 m wide. Image is a Mars Equirectangular projection.

mosaic and overlain with the traverses conducted by Opportunity through sol 561, i.e., to the Fruitbasket outcrop (Figure 5).

[13] The OMEGA false color IR composite, TI, and MOC data show that the Opportunity landing site is located in a portion of the plains with medium albedo and TI relative to surrounding areas (Figures 4 and 5). The surface becomes brighter and redder in the southern portions of the Opportunity traverses and the TI becomes lower (Figure 5). Specifically, the TI is estimated to have a mean of 201 (corresponding to a grain diameter of 160 μm; fine sand [*Presley and Christensen*, 1997]), with a standard deviation of 7 $Jm^{-2}K^{-1}s^{-1/2}$ for the darker, higher TI portion of Opportunity's traverses (northern portion) and values of 193 (corresponding to a grain diameter of 135 μm; fine sand [*Presley and Christensen*, 1997]) and a standard deviation of 9 $Jm^{-2}K^{-1}s^{-1/2}$ for the southerly portion of the traverses. In OMEGA 1183-5 data the region immediately to the south of Opportunity's location on sol 561 is relatively brighter and redder than regions traversed to the north and the MOC-based albedo is higher than for regions traversed up to sol 560 (Figure 5).

[14] Relatively dark regions in the southern Meridiani plains as observed in the MOC WA mosaic correspond to relatively dark red regions in OMEGA false color IR composite (Figure 4). Although not shown, these areas also have relatively low TI values, with a mean of 148 (corresponding to a grain diameter of 45 μm; silt [*Presley and Christensen*, 1997]) and a standard deviation of 8 $Jm^{-2}K^{-1}s^{-1/2}$. The low-albedo pattern extends along the southern and southeastern floor of a large crater located to the south of the Meridiani plains materials. Further, the dark material seems to have been extended to the southeast as a long streak. This extension corresponds to a topographically low area. Also, a number of dark splotches are evident on the southeastern sides of craters floors in the MOC WA data. Bright streaks can also be seen trending from craters to the southeast. Overall the brightness pattern evident in the MOC data is consistent with control by sediment-moving winds from the northwest.

[15] The cratered terrain exposures to the south of the Meridiani plains appear relatively dark and blue in the false color composites as compared to the plains, with a sharp color boundary that corresponds to the southern edge of the plains deposits (e.g., compare Figures 1 and 4). TI data show mean values of 213 (corresponding to a grain diameter of 210 μm; fine sand [*Presley and Christensen*, 1997] – 250 is the cutoff) and a standard deviation of 9 $Jm^{-2}K^{-1}s^{-1/2}$ for the dark regions in the cratered terrain. In OMEGA orbit 171-1, the ejecta deposits from the $\sim$20 km wide crater are relatively dark and "blue," as is the dark splotch on the crater floor. The similarity of the false color patterns for the cratered terrain and the ejecta deposits from the $\sim$20-km-wide crater on the plains reinforces the inference from superposition relationships that the crater excavated into the plains and draped ejecta deposits onto plains materials (Figure 1). This pattern was also identified through analyses of TES data that show the presence of basaltic materials for the ejecta deposits from this crater (P. R. Christensen et al., manuscript in preparation, 2006).

3.4. Surface Reflectance Values

[16] To retrieve surface reflectances from the OMEGA data it is necessary to remove aerosol and atmospheric gas (CO_2, CO, and H_2O) contributions (Figure 3). As noted, we concentrate on the C spectrometer data because these observations are well-calibrated and free from competing influences of reflection of solar radiation and surface emission. In addition, aerosols have much less influence in the C spectrometer wavelengths as compared to the visible portion of the spectrum (Figure 3). Radiative modeling was not used for the retrieval of surface reflectance for

the image cubes, because we do not have exact knowledge of the atmospheric characteristics for regions covered by the OMEGA data, except for the Opportunity site. Instead, gas band effects were removed by scaling relative to OMEGA data acquired from the top of Olympus Mons and the surrounding plains [*Bibring et al.*, 2005]. For wavelengths longer than ~3 μm, OMEGA data are influenced by both solar reflected light and thermal emission from the surface. The emission contribution was removed by using an empirical relationship between the reflectances at ~2 and ~5 μm to estimate emissivity at the longer wavelength, solve for surface temperature, and then remove the effects of thermal emission from the radiance spectra [e.g., *Erard and Calvin*, 1997; *Jouglet et al.*, 2006]. The DISORT-retrieved Lambert Albedo values and the empirically derived surface reflectance values are similar for the Opportunity site and suggest that the approach works, with a slope change for the C spectrometer resulting from removal of aerosol contributions in the DISORT-case. For the short wavelength spectrometer no corrections were done for atmospheric contributions; that is, the values presented as surface reflectance values are the same as the I/F values shown in Figure 3. Detailed analyses of DISORT-corrected spectra for the short wavelength data covering the Opportunity landing site are presented in a subsequent section of this paper.

[17] The next step in analyses of OMEGA data focused on examination of surface reflectance values for each of the units discussed above (Figure 6). The spectral reflectance signatures for the key areas all show strong, broad bands at ~3 μm resulting from the well-known stretching fundamental vibrations of molecular water (ν_1 and ν_3) [*Herzberg*, 1945]. The 3-μm band shapes are similar for all spectra, suggesting that H_2O is contained on surfaces and/or loosely bound in the volume of the materials. Approximately 5% by weight of H_2O is required to explain the spectra based on the modeling approach defined by *Jouglet et al.* [2006]. The lack of H_2O or metal-hydroxide vibrational features between 1 and 2.5 μm identified elsewhere on Mars using OMEGA data [e.g., *Bibring et al.*, 2005; *Gendrin et al.*, 2005; *Arvidson et al.*, 2005; *Poulet et al.*, 2005] argues against the presence of possible hydrated sulfates or phyllosilicates. This inference is consistent with the relatively few surface exposures of sulfate-rich outcrops and the dominance of basaltic sands and hematitic concretions observed by Opportunity on the plains [*Squyres et al.*, 2004a] and is supported by examination of spectra normalized to nonplains spectra (e.g., cratered terrain exposures to the south).

[18] All OMEGA spectra have steep slopes shortward of ~0.80 μm, consistent with the ubiquitous presence of nanophase iron oxides and associated ferric absorptions [e.g., *Bell et al.*, 1993; *Morris et al.*, 2000]. Spectra for the dissected cratered terrain and ejecta deposits from the ~20-km crater on the plains (southwest of landing site) both show shallow absorptions at ~1 and ~2.2 μm, consistent with spectral dominance by pyroxene [*Adams*, 1975]. The Opportunity site spectrum exhibits a broad peak at ~1.6 μm, consistent with absorptions resulting from pyroxene at shorter and longer wavelengths, but not as deep as those seen for the cratered terrain spectra. The bright plains immediately to the south of the landing site are spectrally similar to the plains surrounding Opportunity but with a higher overall reflectance. Note that the spectrum for the dark red plains to the south of Opportunity has a low magnitude overall relative to the landing site and a slightly higher slope from 0.9 to ~1.3 μm. The bright terrain spectrum to the north of the landing site is typical for bright areas on Mars and has similar spectral patterns as fine-grained dust rich in nanophase iron oxides [e.g., *Bell et al.*, 1993; *Morris et al.*, 2000].

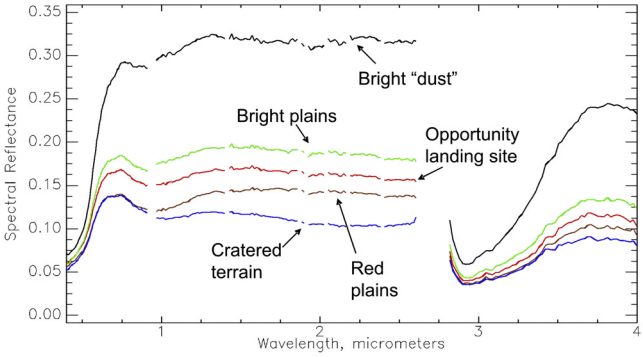

Figure 6. Surface reflectance values are shown for OMEGA spectra for locations in 1183-5 shown in Figure 4. I/F values were used for the VNIR channels (0.4 to 1.0 μm). For the C spectrometer gas bands were removed on the basis of scaling relative to observations from the top to the plains surrounding Olympus Mons [*Bibring et al.*, 2005]. Data for the 171-1-based end-member are not shown to avoid clutter, but exhibit trends similar to those for the cratered terrain spectrum. A bright dust spectrum was added to the end member set shown in Figure 4. This spectrum is located at 1.79°N and 354°E, and is typical of low-inertia bright areas. Detailed analysis of spectra is discussed in the text.

3.5. Retrieval of Mineral Abundances

[19] The next step in analysis of the OMEGA spectra is quantitative retrievals of mineral abundances, using the visual interpretations presented above as a guideline and restricting our modeling to the well-calibrated C spectrometer data. Specifically, visual inspection shows that the spectra are controlled by charge transfer and electronic transition bands involving ferrous and ferric iron and not by vibrational features, except for the water vibrations at ~3 μm (Figure 6). Thus modeling is restricted to the likely minerals present based on inspection of the spectra and the documented presence of particular mineral species identified from Opportunity observations. The minerals used in the retrievals are olivine and pyroxene, which control the shape of the spectra, and feldspar, crystalline hematite, and dust, which modulate the overall albedo. The intent is to estimate relative proportions and grain sizes of these materials for the Opportunity site, the bright plains and dark red plains, and the cratered terrain spectra (Figure 6) using Shkuratov radiative transfer theory [*Shkuratov et al.*, 1999]. This geometrical optics model is based on a slab approximation for calculating the albedo of a particle and has been compared to other scattering models [*Poulet et al.*, 2002] and tested with laboratory mineral mixtures [*Poulet and Erard*, 2004].

[20] The Shkuratov model, as well as other scattering models, relies on the knowledge of the optical constants of the mineral components. The optical constants are derived using the method described by *Poulet and Erard* [2004] from the following spectral reflectance data: Clinopyroxene (diopside), orthopyroxene (enstatite) and olivine (forsterite) are based on Keck/NASA RELAB spectra from *Pieters et al.* [1993], plagioclase (labradorite) is based on spectra from ID PL-CMP from RELAB, provided by C. Pieters (unpublished data, 2006), crystalline hematite data are from *Lane et al.* [2002], and dust data are derived spectra for dehydrated palagonite from Pu'u Nene cinder cone (Hawaii; RELAB sample ID CC-JFM provided by J. F. Mustard (unpublished data, 2006)). As noted in this paper, aerosols modestly affect the spectral slopes. Thus one additional free parameter is used to modestly adjust the continuum spectral slope. The optimization of abundances and grain sizes of each end-member was calculated using a downhill simplex technique [*Poulet and Erard*, 2004]. Crystalline hematite, plagioclase, and dust spectra are spectrally flat, making it difficult to estimate their relative abundance with an uncertainty of better than 10 to 20% (by volume). By contrast, olivine and pyroxenes have strong absorption bands in the wavelength range under consideration and their abundance are well derived (<5%). Results for the slab modeling are shown in Figure 7 and Table 2 and summarized in the following paragraphs. We focus on mineral inferences, although we note that grain size retrievals are within a factor of 2 for values estimated from TI (previous section of paper) and are within the accuracy of the technique used to estimate grain size [*Poulet and Erard*, 2004]. The model does not reproduce hematitic concretion size well, because these spherules are sitting on the surface rather than embedded within the sands, i.e., a violation of model assumptions.

3.5.1. Cratered Terrains

[21] Results for OMEGA orbits 1183-5 and 171-1 are very similar. Both low-calcium (LCP) and high-calcium (HCP) pyroxene are required in a relative proportion of 1/4. Olivine is not retrieved from the modeling. A spectrally neutral material is required to match the data and is best represented by the plagioclase component. The mineral abundance is in a proportion similar to the TES-derived Type I spectra found in the cratered terrains [*Bandfield et al.*, 2000; *Hamilton et al.*, 2001; *Bandfield*, 2002]. Inferred grain sizes are in the medium to fine sand size range.

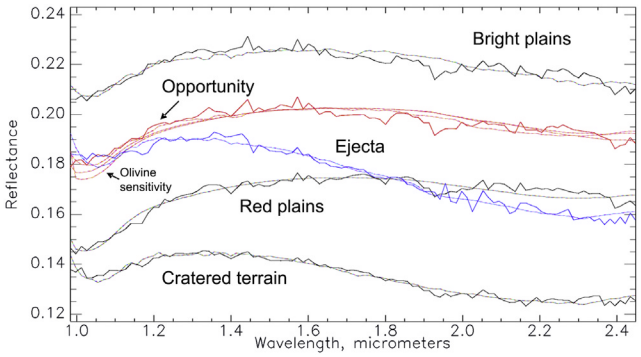

Figure 7. OMEGA C spectrometer data for key sites and associated models as discussed in the text. No olivine is retrieved in the nominal model for the Opportunity site. Two dashed lines above the label "olivine sensitivity" correspond to inclusion of 5% (upper line) and 10% (lower line) olivine. Ejecta are from OMEGA orbit 171-1. Other data are from orbit 1183-5.

Table 2. Results From OMEGA Mineral Abundance Retrievals

	CPX	OPX	Crystalline hematite	Dust	Olivine	Plagioclase
Cratered Terrain, RMS = 0.00158						
Grain size, μm	80	50–100		10	10	50–100
Abundance, Vol%	25	7		<5	<5	60
Crater Ejecta Deposits, RMS = 0.0022						
Grain size, μm	50	50		10		100
Abundance, Vol%	30	5		10		50
Opportunity Landing Site, RMS = 0.0026						
Grain size, μm	20		200–400	10		100–200
Abundance, Vol%	30		20	15		30
Brighter Region (South of Landing Site), RMS = 0.0028						
Grain size, μm	20		200–400	10		100–200
Abundance, Vol%	25		15	25		35
Southern Red Plains, RMS = 0.0021						
Grain size, μm	20		500	10	15	100
Abundance, Vol%	25		25	10	15	25

3.5.2. Opportunity Site

[22] The spectrum is well reproduced by a mafic sand (grain sizes dominated by values smaller than 100 μm) mixed with crystalline hematite particles with diameters of several hundreds of micrometers. Only a small amount of dust is allowed on the basis of the low overall reflectance. Olivine is not retrieved in the modeling. In fact, an addition of only ~5% of olivine significantly enhances the 1-μm olivine band and is inconsistent with the spectrum for the Opportunity site (Figure 7). Although it is difficult to constrain the relative proportion of plagioclase and hematite, their abundances are significant and serve to reduce the pyroxene absorption band depths.

3.5.3. Bright Terrain South of Opportunity

[23] For brighter terrain south of the landing site an enhanced dust component is needed to match the observed spectrum, together with the same materials found at the Opportunity site.

3.5.4. Dark Red Plains in Southern Meridiani Planum

[24] The dark red plains spectrum requires the presence of silt-sized olivine and pyroxene to reproduce the 1-μm band depth and shape. The fine grain sizes from the retrievals are consistent with the low TI for this region (Figure 5). It is important to note that the shape and depth of the 1-μm band could be explained by the presence of other Fe^{3+}-bearing minerals which were not included in the end members used in the models because of a lack of optical constant information. However, the simplest interpretation, using the minimum number of end members, is that the dark red plains are enhanced in the relative abundance of silt-sized olivine compared to other areas of the plains.

4. Opportunity Observations and Analyses

4.1. Overview

[25] The intent of this section is to compare observations from the Opportunity rover with results inferred from the OMEGA, MOC, and THEMIS data covering the landing

Table 3. Summary of Post-Endurance Opportunity Activities[a]

Sol	Activity
315–325	Egress Endurance Crater; *MI tracks* on 319; drive to Heat Shield
326–359	Heat Shield measurements and remote sensing; Heat Shield Rock 347-352
360–366	drive and excavate sol 366 trench south of Jason
367–373	*trench and scuff MI, MB, APXS measurements*
374–376	software upload
377–378	remote sensing and drive
379–380	*Russett rock MI, MB, APXS measurements*
381–388	drive and remote sensing
389–395	*Normandy MI, MB, APXS* and remote sensing
396–403	*Gagarin rock target and Laika Soil Target MI, MB, APXS Vostok* on sol 399
404–414	drive and remote sensing
415–420	*drift crest and valley MI, MB, APXS Mobarak, Nobrooz, Mayberooz*
421–429	drive and remote sensing of plains, Viking and Voyager Craters
430–438	drive and remote sensing; 433 right front wheel azimuth stall and diagnostics
439–440	turn to comm scuff imaging; software reboot
441–445	*MI, MB, APXS of comm. scuff*; drive
446–484	drive into and extrication from Purgatory ripple
485–515	Purgatory ripple experiments
516–542	drive and remote sensing
543–561	*Fruitbasket outcrop and cobble MI, MB, APXS*

[a]Italics denote when in situ observations with the Instrument Deployment Device (IDD) were made.

site (Figures 1–7 and Table 3). As noted, data collected by the Opportunity rover for soil deposits and rock outcrops in Eagle and Endurance craters, together with observations acquired as the vehicle traversed across the plains, show that the hematite-bearing plains materials are dominated by poorly sorted basaltic sands littered with granule-sized crystalline hematitic concretions (1 to 4.5 mm) [*Arvidson et al.*, 2004; *Soderblom et al.*, 2004; *Squyres et al.*, 2004a, 2004b; *Weitz et al.*, 2006]. Large parts of the surface are also covered by ripples composed of whole and broken hematitic concretions [*Sullivan et al.*, 2005; *Jerolmack et al.*, 2005]. The ripple crests are covered with high concentrations of hematitic concretion spherules and their fragments [*Klingelhoefer et al.*, 2004; *Morris et al.*, 2006]. The underlying rocks, exposed in crater walls and as patches in the plains, are dominated by sulfates postulated to have formed in a ''playa-like'' evaporative environment, followed by reworking by water and wind and subsequent ground water diagenesis [*Squyres et al.*, 2004b; *Grotzinger et al.*, 2005]. In particular, the hematitic concretions are interpreted to have formed by diagenesis after burial of the sulfate-rich rocks [*McLennan et al.*, 2005] and have concentrated on the surface as aeolian lags and granule ripples as the softer sulfate-rich rocks were preferentially eroded by winds. The basaltic sand and hematitic concretion lag/rippled surface, with scattered outcrops, dominates the view observed from orbit for the landing site and immediate vicinity, and detailed results from these plains observations and analyses of relevance to comparisons with orbital results will be pursued in the paragraphs that follow. We focus on the traverses that extend from the period when the rover left Endurance crater on sol 351 to when it left the Fruitbasket outcrop on sol 562 (Table 3). The reason is that the southerly traverses between these two sites occurred over terrain with smoothly varying values in spectral properties, albedo, and thermal inertia (Figure 5), and because science operations focused on systematic documentation of the plains surfaces using the Athena Payload. Thus a comprehensive data set was collected that can be used to retrieve mineralogy and textural information for comparison with inferences from orbital observations (e.g., Table 2).

4.2. Wheel Tracks

[26] After Opportunity exited Endurance crater, the vehicle was commanded on sol 317 to cross a set of tracks made during the initial approach to the crater on sol 131 so that material disturbed by the rover wheels and exposed to ambient conditions for 186 sols (Figures 8 and 9) could

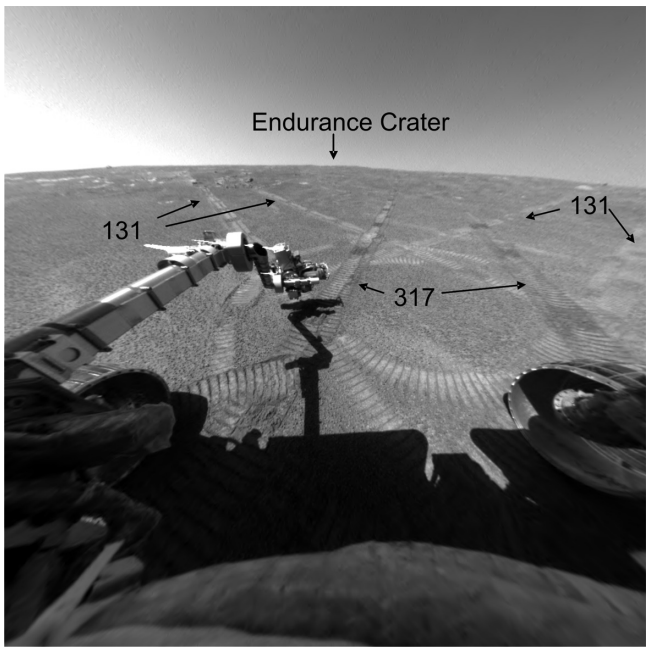

Figure 8. Hazcam view from sol 319 of wheel tracks generated on sols 131 and 317, as Opportunity traversed toward and away from Endurance crater, respectively. Instrument deployment device is shown acquiring MI data over an older track. Frame number is 1F156502857FFL3940P1110L0M1.

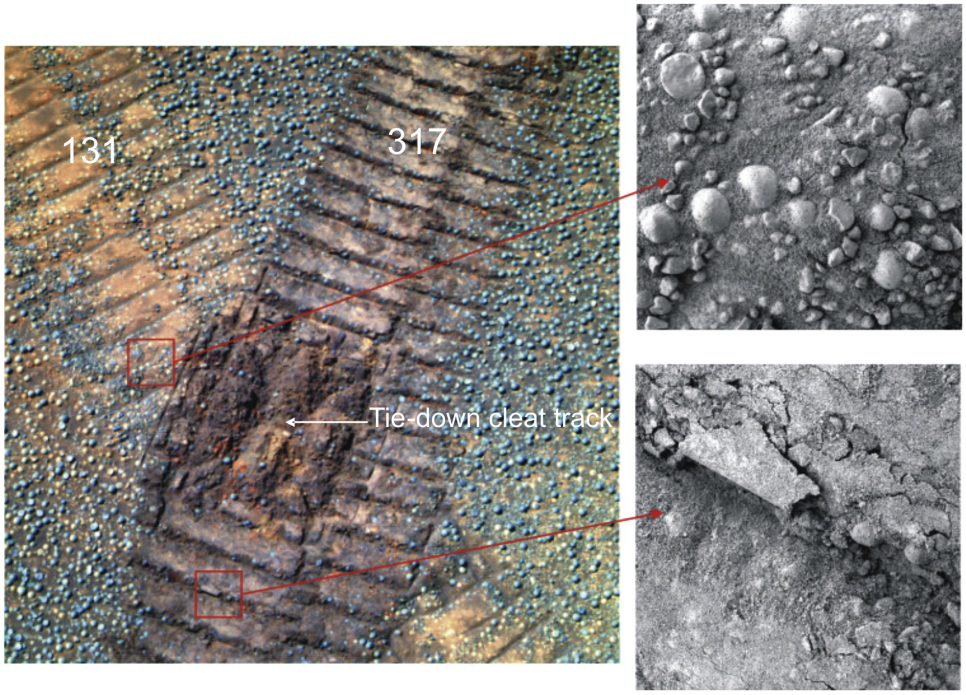

Figure 9. Pancam and Microscopic Imager (MI) views of new and old tracks. Pancam frames acquired on sol 319. Pancam frames, wavelengths, and color assignments in this and subsequent figures are: 1P15650173EFF3940P2571L7C1 (440 nm, blue), 1P1565016484EFF3940P2571L5C1 (535 nm, green), 1P156501597EFF3940P2571L2C1 (753 nm, red). MI frames: 1M156502307EFF3940P2977M2F1 (old track) and 1M156503270EFF3940P2977M2F1 (new track). Both MI targets were acquired when fully shadowed. Wheel track widths are ~15 cm wide and MI images cover ~3 cm in width and height. Note that younger tracks expose dark material and appear to have disrupted a bright red soil crust (clods are present). Disrupted zone in the new track is associated with wheel cleat used for tying down the rover to the lander. Older track impressions are smooth, bright, and red as compared to the new tracks. Note the finely molded nature of the new tracks, suggesting a poorly sorted material in which fine grains (<0.1 mm) fill interstices within the soil, allowing the material to retain a shape during deformation. Both bright red and dark, gray patches are evident on undisturbed surfaces between the hematitic concretions.

be studied. The undisturbed surfaces surrounding the tracks are littered with granule-sized hematitic concretions (Figure 9) in a manner similar to what was observed by Opportunity on the plains during its traverses from Eagle to Endurance craters [*Soderblom et al.*, 2004; *Sullivan et al.*, 2005]. Note that the concretions disturbed by the tracks have been pushed into the sands by the wheels, implying relatively weak substrate materials. For both sets of tracks the surface has been molded by the wheel cleats, suggesting that the deposits are relatively easily deformed and retain the molded shapes. This soil behavior is consistent with poorly sorted materials, including sand-sized particles that can be seen in the MI images (~100 to several hundred μm grain sizes), and what is probably unresolved finer-grained material that fills pore spaces and allows the sands to be molded by the wheels [*Arvidson et al.*, 2004]. Bright red clods are evident in the younger tracks suggesting disruption of a slightly indurated soil layer. The older tracks are bright and red and have smoothed edges relative to the younger tracks. These observations are consistent with aeolian removal of loose darker material (probably as saltation load) and exposure of a bright red indurated soil over the relatively short period of 186 sols between formation of the older tracks and imaging from the rover. The undisturbed substrate on which the concretions sit has a mottled pattern of relatively bright red and dark gray areas, consistent with the presence of dark, loose materials over a bright red surface crust. The dark, loose component is interpreted to be poorly sorted basaltic sand.

4.3. Trenching Experiment

[27] Between sols 360 and 373 the rover excavated a ~10-cm-deep trench with a long dimension that is perpendicular to the strike of one of the ubiquitous aeolian ripples on the plains (R. Sullivan et al., manuscript in preparation, 2006) (Figures 10 and 11). Pancam and MI data show that the undisturbed ripple trough adjacent to the trench is covered with patchy bright red and dark gray areas and the ubiquitous lag of hematitic concretions. The overall appearance of the surfaces is indeed similar to what was observed in the crossing tracks undisturbed surfaces observed on sol 319. The ripple crest is covered with an areally dense array of concretions that is one layer thick and smaller in grain size (~0.3 rather than 3 mm) than the interripple concretions. This pattern has been interpreted to result from preferential wind transport of smaller concretions onto ripple crests [*Jerolmack et al.*, 2005]. The interior of the ripple and the bulk of the soil exposed by trenching

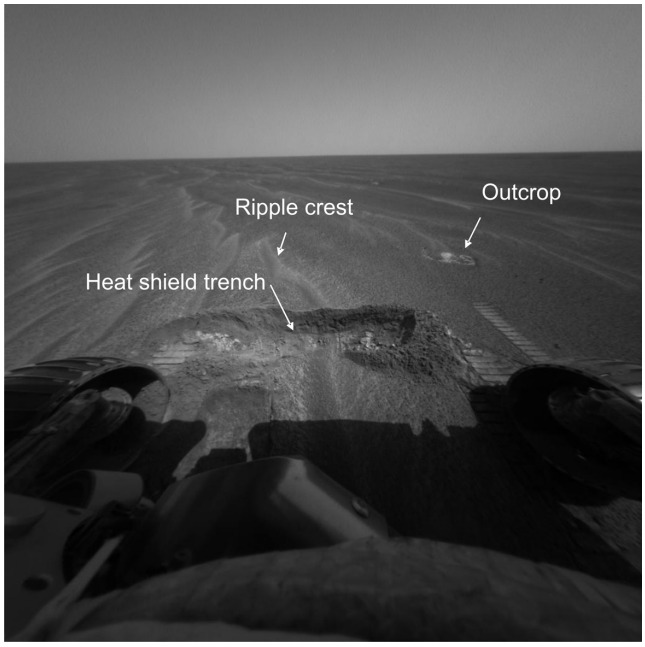

Figure 10. Hazcam view of sol 366 trench excavated near Opportunity's heat shield. Trench depth is ~10 cm. Note that the trench was purposely excavated to expose material beneath an aeolian ripple crest. Small patch of outcrop is delineated by arrow in image. Frame number is 1F160676950FFL42D9P1214LOM1.

consist of what appears to be a thin bright red crust at the top and beneath this zone a poorly sorted sand. The poorly sorted nature of the sand is inferred from MI images and the fact that the MB contact plate was able to finely mold the soil (Figure 11). The ripple crest and trough pattern is typical of the surfaces encountered by the vehicle on its traverses south, including a stop to make detailed measurements on ripple crests and troughs on sols 415–419 (Figures 12 and 13). In this case, MI images were acquired that reinforce the notion that relatively fine-grained hematitic concretions are concentrated on ripple crests whereas the troughs are littered with more widely spaced hematitic concretions sitting on a substrate of relatively dark crystalline and bright red materials. This observation is clearly documented by MB results, which show the highest concentrations of hematite at ripple crests [*Klingelhoefer et al.*, 2004; *Morris et al.*, 2006].

4.4. Purgatory Ripple and Fruitbasket Outcrop

[28] On sol 446 Opportunity was conducting a drive using its auto-navigation system to avoid obstacles. As the rover attempted to ascend the flank of a ~25-cm-high ripple (subsequently named "Purgatory ripple"), the vehicle encountered nearly 100% slip as the rear wheels (it was driving backward by design) became embedded into ripple material up to the wheel tops. After a number of sols trying to back out of the ripple, the rover was extricated and an extensive measurement campaign was undertaken. Measurements were made within the tracks generated on sol 446 and the new tracks made on sol 491 once the rover was extricated from the ripple (Figure 14). Pancam images of undisturbed areas near the wheel tracks show the typical pattern of hematitic concretions and a substrate of bright red and dark gray materials. MI data show that the MB contact plate made very finely detailed molds within the materials exposed within the tracks, with less granular texture evident as compared to MI images in the trench excavated to the north (Figure 11). The contact plate results imply a greater concentration of fine-grained material as compared to the sol 366 contact plate results.

[29] After completing experiments within and near the Purgatory ripple, the rover continued its traverse south toward Erebus crater (Figure 5). On sol 555 the rover approached an interripple outcrop called Fruitbasket (Figure 15). A strewn cobble field was located nearby. Both outcrop and cobbles were examined in detail. Outcrops were found to increase in areal extent as the vehicle traversed from Purgatory to Fruitbasket. Ripples typically became higher in amplitude and exhibited eroded bright crests (Figure 15). These observations correspond to locations where OMEGA and MOC brightness values increase, whereas TI values decrease. It is hypothesized that the lower TI results from the presence of ripples with smaller concretions [*Weitz et al.*, 2006] and finer overall grain size of the aeolian bedforms, with enough of an effect to counter the increased areal abundance of outcrop, which should have a higher TI than soils.

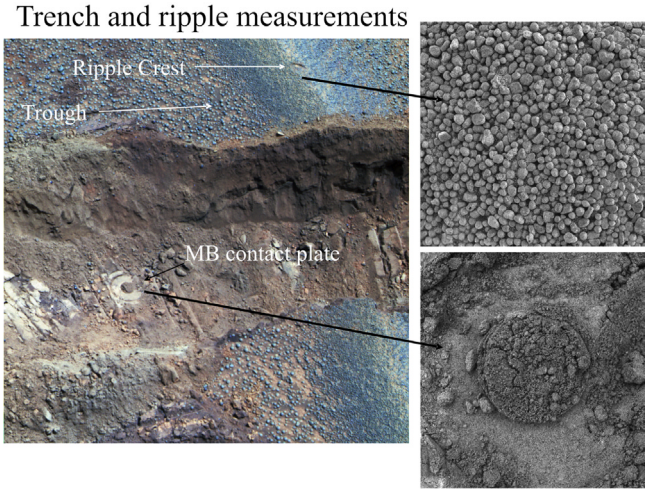

Figure 11. Pancam and MI views of the sol 366 trench and areas analyzed using IDD instruments. Ripple crest is densely covered by hematitic concretions whereas the trough is covered by a less dense array of larger hematitic concretions, with bright red and dark substrate exposed. The steep trench wall, clods, and the mold due to placement of the MB contact plate imply that the exposed soil is slightly coherent and poorly sorted. MI images show sand and finer-grained materials are present. Pancam frames acquired on sol 372 are: 1P161207836EFF42DIP2374L2C1, 1P161207869EFF42DIP2374L5C1, 1P161207895EFF42DIP2374L7C1. MI frames acquired on sol 368 are: (top) 1M160851916EFF42D9P2997M2F1 and (bottom) 1M160851441EFF42D9P2997M2F1, both acquired when the targets were fully shadowed. MI images cover ~3 cm in width and height.

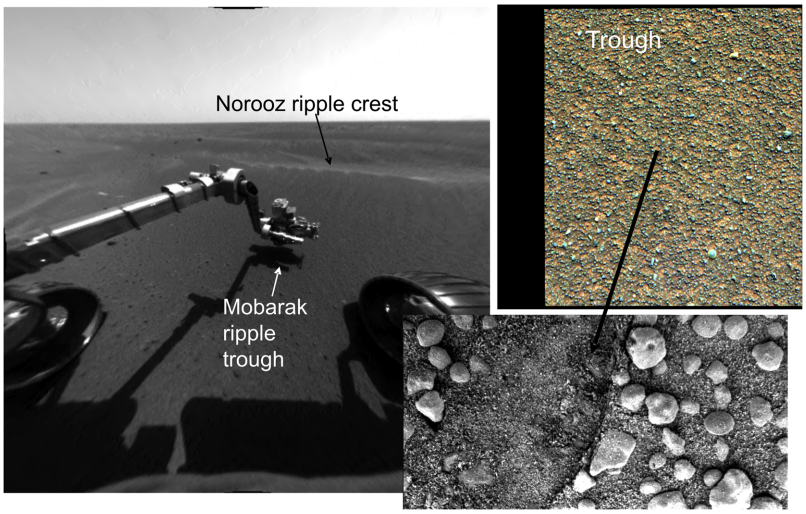

Figure 12. Hazcam, Pancam, and MI views of Mobarak ripple trough. Note that the trough is covered with ubiquitous hematitic concretions and a substrate of bright red and dark surfaces. MI image shows the sandy nature of the substrate with the well-defined MB contact plate imprint, implying the presence of a fine-grained component. Comparison of MI data from Mobarak and MI data acquired on exiting Endurance (Figure 9) show that concretions have similar sizes. Frames are as follows: Hazcam: 1F165026335DNL5200P1111ROM1; Pancam sol 415: 1P165024166ESF5200P2584L7C1, 1P165024094ESF5200P2584L5C1, and 1P165024011ESF5200P2584L2C1; MI: part of 1M165026076EFF5200P2956M2F1, acquired when target was fully shadowed.

4.5. APXS and MB Observations

[30] Elemental (APXS) and iron mineralogical (MB) measurements conducted during the traverses from Endurance crater to the Fruitbasket outcrop provide additional and important information on the characteristics of material encountered on the plains. Detailed presentation and analysis of APXS and MB data for Opportunity are presented by R. Gellert et al. (manuscript in preparation, 2006) and *Morris et al.* [2006]. The approach taken in this paper is to reduce the dimensionality of derived data from these papers using correspondence analysis (CA), which is an approach adopted by *Arvidson et al.* [2006] to describe similar data acquired by the Spirit rover. CA is a normalized principal components rotation that allows factor loadings associated with variables and samples to be plotted together. The first two eigenvectors for APXS data, expressed as oxide concentrations, explain 94% of the variance in composition (Figure 16). In particular, the sulfate-rich nature of outcrops is evident from the strong correlation between measurements on the Gargarin outcrop in natural state, after brushing, and then after a RAT operation removed ~5 mm of the outer portion of the target. The Gargarin outcrop was encountered in Vostok crater and was examined in order to search for changes in rock composition and mineralogy

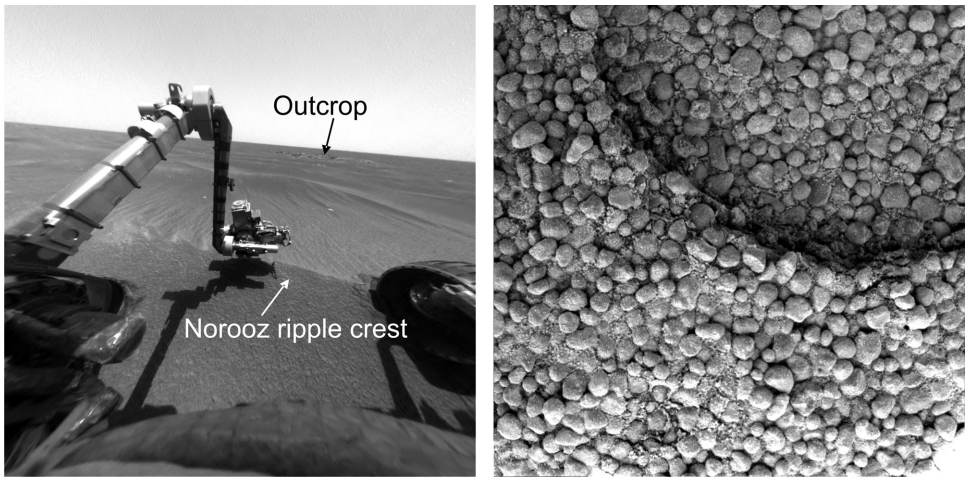

Figure 13. Hazcam and MI views of Norooz ripple crest. Note high areal concentration of relatively small concretions on crest. Hazcam frame number is 1F165379910FFL5208P1110L0M1; MI frame number is 1M165379575EFF5208P2956M2F1, acquired while target was fully shadowed. MI image covers ~3 cm in width and height.

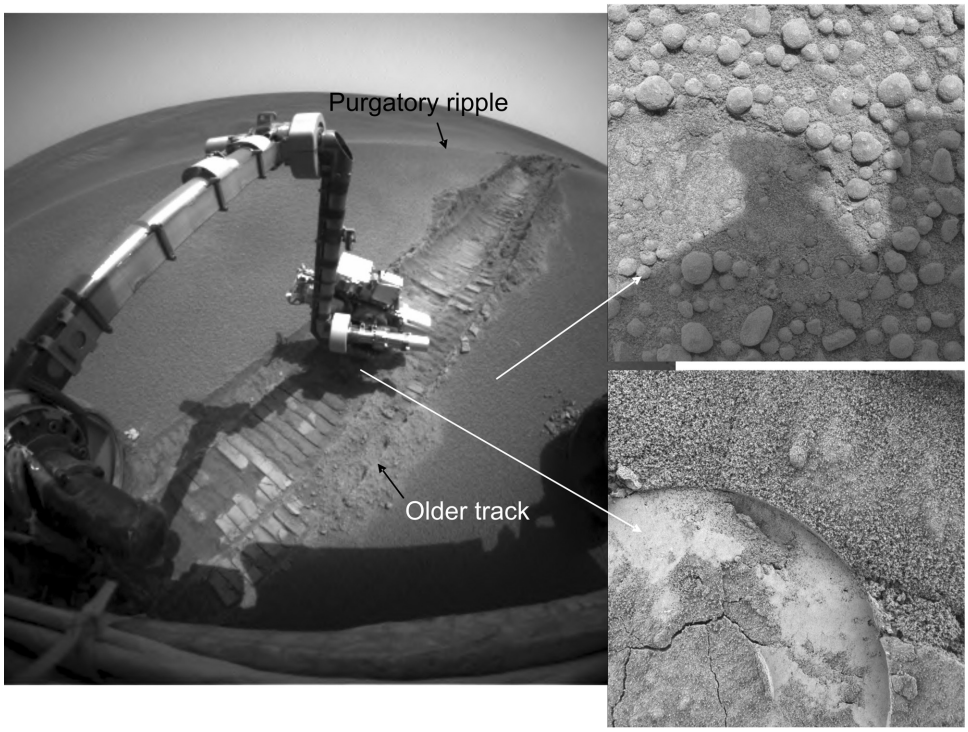

Figure 14. Hazcam and MI views of Purgatory ripple after Opportunity backed out. Very well defined molds are evident, consistent with a relatively high abundance of fine-grained materials. Ubiquitous hematitic concretions are still evident for the undisturbed surface. Older track where exposed is brighter than the younger track, probably because of dust deposition. Note the shadow of the IDD turret at the top of upper MI frame. Bottom MI frame was acquired while target was fully shadowed. Hazcam frame number is 1F173279793EDN55W4P1131L0M1; MI frames acquired on sol 507 are (top) 1M173191578EFF55W4P2956M2F1 and (bottom) 1M173193890EFF55W4P2936M2F1. MI images cover ~3 cm in width and height.

relative to outcrops to the north (Figure 5) (Squyres et al., submitted manuscript, 2006). APXS data for Gagarin show that the SO_3 content increases systematically from the outer surface to the inner, ratted surface and the overall trend is to move the results away from the swarm of data indicative of basaltic materials. The brushing and grinding thus removed a ''contamination'' of basaltic sand from outcrop surfaces. The APXS data also show that the three cobbles examined during the southward traverses from Endurance crater are compositionally variable. Russett cobble (near the Gargarin outcrop) is possibly derived from the nearby outcrop. Arkansas and Perseverance cobbles near the Fruitbasket outcrop (Figure 15) have a more mafic composition.

[31] CA plots for APXS results show a strong linear trend for soils defined by trench and scuff oxide and ripple crest end-members, with interripple trough materials located between these two extremes (Figure 16). Normative mineral calculations show that the trench, scuff, and Purgatory track data correspond to olivine-normative basalt, although the fact that the material is a mechanical (i.e., wind) mixture precludes definitive estimation of the relative abundances of olivine and its iron content (i.e., the calculations are specific for igneous rocks). The high iron oxide content of the ripple crests is consistent with a dominance of hematite concretions. The interripple troughs are consistent with a mix of iron oxides (concretions), basaltic sand (dark crystalline surfaces), and dusty materials (bright red surfaces).

[32] MB results reinforce the conclusions that outcrop is dominated by sulfate minerals (jarosite is detected by the MB, [*Klingelhöfer et al.*, 2004; *Morris et al.*, 2006]), cobbles vary in mineralogy but have sulfate components, and soils have a distinctly different pattern (Figures 17 and 18). In particular the iron in trench and scuff analyses shows a strong affinity for pyroxene, magnetite, and olivine, whereas the ripple crests are dominated by hematite and a subordinate amount of olivine. Ripple troughs are intermediate between these two end-members. In addition, the measurements from the Purgatory ripple track show an enhancement of nanophase ferric oxides as compared to the sol 366 trench and scuff (Figure 18), consistent with MI data that the material has a relatively high proportion of fine-grained materials.

4.6. Mini-TES and Pancam-Based Spectra

[33] Mineral retrievals above the 10% level obtained for Mini-TES observations of plains examined between Eagle and Endurance craters include crystalline hematite, plagioclase feldspar, sulfate minerals, and clinopyroxene [*Christensen et al.*, 2004b]. Olivine was detected as a minor phase. Unfortunately, dust on the Mini-TES mirror has hampered analyses of plains measurements acquired after exiting Endurance crater. However, a technique to remove this effect from Mini-TES data has been implemented at the Spirit landing site, and a similar method is being developed

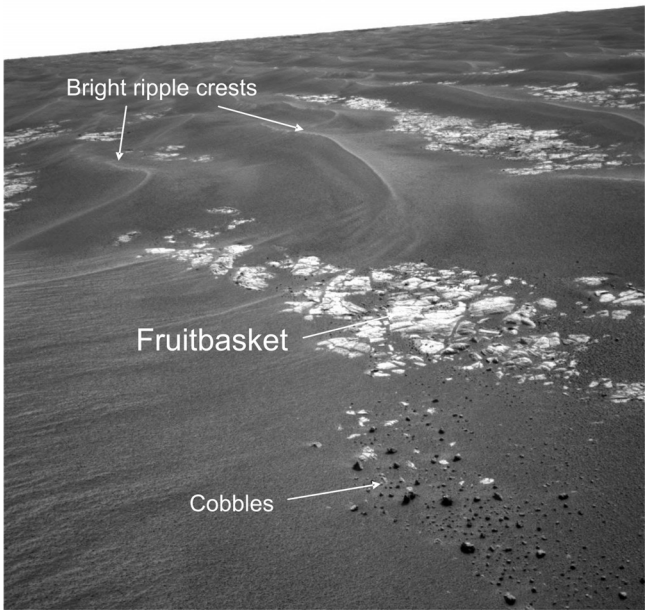

Figure 15. Navcam image of Fruitbasket outcrop and surrounding ripples. Outcrops are more abundant in ripple troughs to the south of the Purgatory ripple. Note also the bright crests of the ripples, consistent with a greater relative abundance of dust in these ripples as compared to those encountered to the north. Cobbles are exposed to the bottom of the image. Frame number is 1N176930758FFL58CXP0713L0M1.

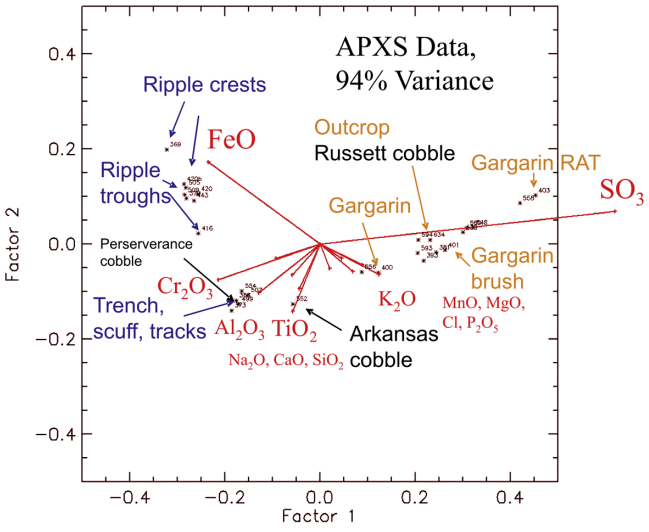

Figure 16. Scatterplot from correspondence analysis applied to APXS data from the plains between Endurance crater and the Fruitbasket outcrop. The first two factors explain 94% of the variance in samples. Note the correspondence between the SO_3 content and outcrop materials, including higher SO_3 with increasing depth in the outcrop target, Gargarin. Ripple crests have high FeO due to hematitic concretions, whereas the trench and scuff material show a more complex correspondence with a composition typical of basalts. Ripple troughs fall between these extremes.

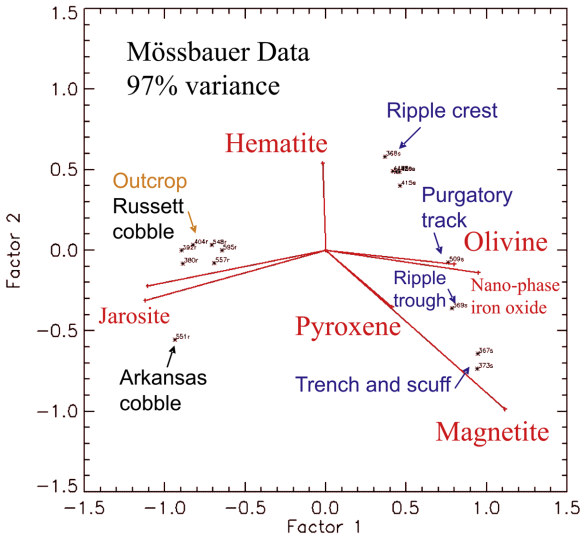

Figure 17. Scatterplot from correspondence analysis applied to MB data from the plains between Endurance crater and the Fruitbasket outcrop. The first two factors explain 97% of the variance in samples. Outcrops are dominated by jarosite. Note the linear trend from ripple crests to trench and scuff materials and the correspondence with hematite and basaltic minerals, respectively.

for Opportunity data by the Mini-TES team (D. Rogers, personal communication, 2006).

[34] The final data sets to be examined are the Pancam 13 filter multispectral observations that were acquired from 0.4 to 1.0 μm for a number of targets during traverses and

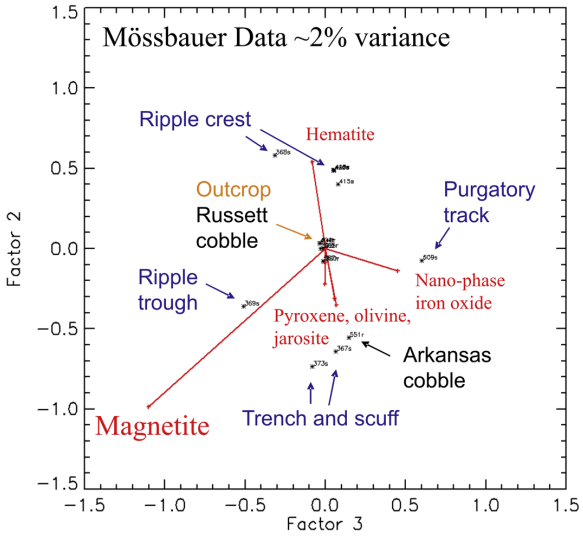

Figure 18. Scatterplot from correspondence analysis applied to MB data from the plains between Endurance crater and the Fruitbasket outcrop. The second two factors explain ~2% of the variance in samples. The projection is perpendicular to the factors 1 and 2 scatterplot shown on Figure 17. The Purgatory ripple track observation is skewed toward nano-phase iron oxides relative to the dominant hematite-pyroxene-olivine-jarosite trend. The ripple trough value is displaced toward enhanced magnetite.

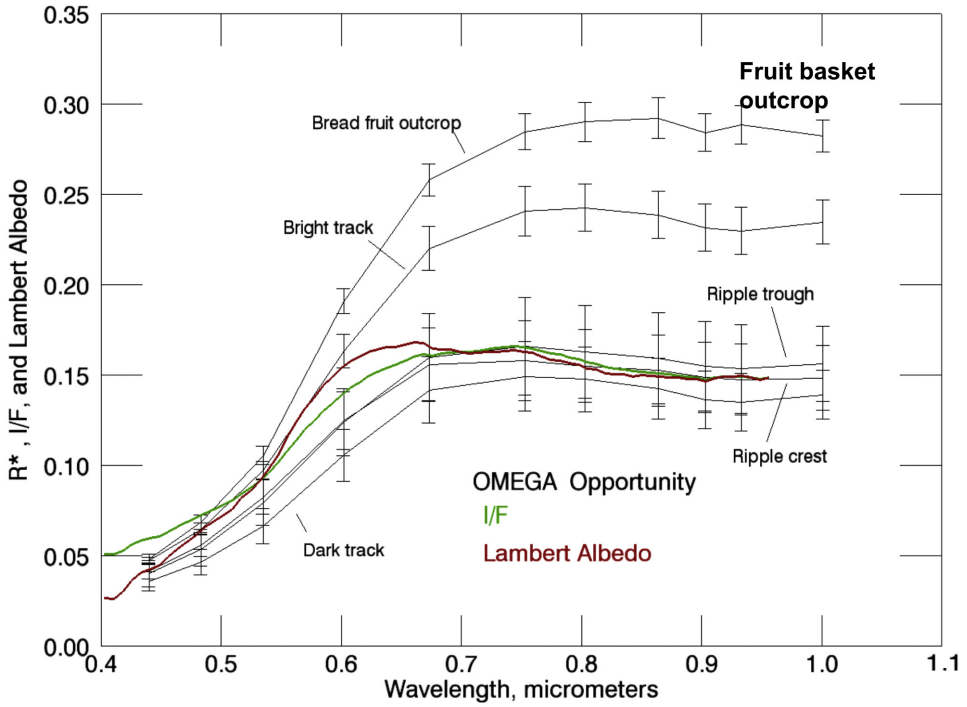

Figure 19. Pancam R* spectra for old and new tracks, natural surfaces, and the Fruitbasket outcrop. Also shown are surface reflectance values and retrieved Lambert albedos from OMEGA VNIR spectrometer 1183-5 data for the areas traversed by Opportunity. Error bars are 1 standard deviation about mean value.

experiments conducted by Opportunity between Endurance crater and Fruitbasket outcrop. The Pancam data were reduced to R* values using the calibration target on the rover deck [*Bell et al.*, 2004]. These values are comparable to Lambert albedos and are shown in Figure 19. The spectrum for the dark track acquired on sol 131 is the darkest one shown and shows a band minimum at ~0.93 μm, consistent with the presence of pyroxene [*Bell et al.*, 2004]. The bright track spectrum also shows this band, as does the ripple trough spectrum. By contrast, the ripple crest spectrum does not show this feature, consistent with the abundance of crystalline hematite concretions on ripple crests. The Fruitbasket outcrop spectrum shows a shallow band at 0.89 μm and an inflection at 0.54 μm, consistent with the presence of red, fine-grained hematite known from MB observations to be a component of this outcrop [*Klingelhoefer et al.*, 2004; *Morris et al.*, 2006].

[35] Figure 19 also shows the I/F spectrum for the Opportunity site from OMEGA data and a nominal retrieved Lambert albedo spectrum for the OMEGA coverage, using the atmospheric parameters defined previously. The retrieved surface spectrum has a steeper slope in the visible than the I/F spectrum because: (1) the effects of additive skylight have been removed at the shortest (and darkest) wavelengths, and (2) the longer wavelength, brighter portion of the spectrum has the effects of surface radiance attenuation removed. The retrieved OMEGA Lambert albedo spectrum corresponds most closely to ripple and interripple trough spectra, two surface types that dominate the plains in areal extent. This correspondence between the OMEGA and Pancam data reinforces the notion that rover-based observations can be used to understand in detail the signatures observed from orbit for the Meridiani plains.

[36] Pancam, OMEGA, and Mini-TES spectra show strong bands associated with pyroxene and little evidence for abundant olivine. This result is seemingly inconsistent with MB results that indicate subequal proportions of iron associated with olivine and pyroxene. On the other hand, it is well known that olivine and pyroxene mixtures produce reflectance spectra that are non-linear mixtures with a bias toward spectral features of pyroxene [e.g., *Singer*, 1981]. The reason is that olivine is clear and euhedral, whereas pyroxene is platy and has internal interfaces for enhanced backscatter. The addition of dust can further obscure olivine or pyroxene features in reflectance spectra. We illustrate this situation by experiment, using naturally occurring olivine and glass-bearing tephra from Mauna Kea, which naturally contains variable proportions of palagonite and olivine (Figure 20). The size fraction with ~30% each of iron in olivine and npOx has the approximate shape and amplitude as the Pancam-based dark track spectrum, but only barely shows evidence for the short wavelength portion of the ~1-μm olivine bands. Higher relative abundances of dust obscure the bands completely. In summary, we do not see a discrepancy between the reflectance and MB results for the Opportunity site. Additional work beyond the scope of this paper is needed to incorporate Mini-TES results.

5. Synthesis and Implications for the Origin and Evolution of Terra Meridiani

[37] Cross comparisons of OMEGA and Opportunity observations demonstrate that the plains of Meridiani are

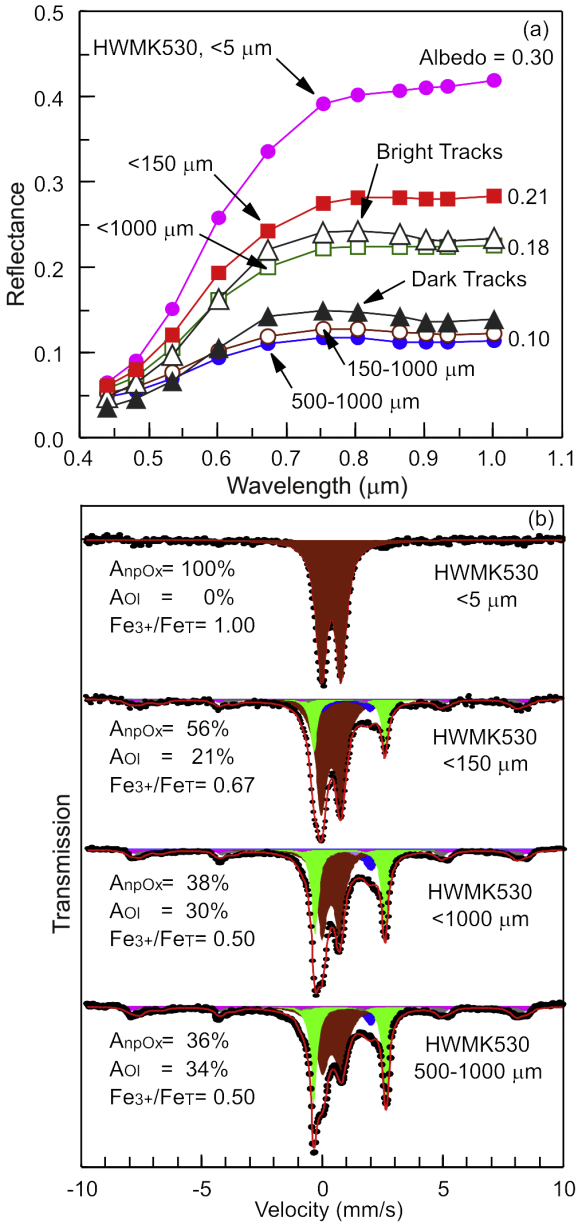

Figure 20. (a) Pancam multispectral data for old (dark) and new (bright) tracks and Pancam equivalent spectra for five size fractions of palagonitic tephra HWMK530 (<5, <150, 500–1000, and <1000 μm as defined by *Morris et al.* [2000]). HWMK530 spectra are characterized by a ferric absorption edge (~0.44–0.75 μm) and nearly constant reflectance at longer wavelengths, and there are no detectable band minima. Pancam multispectral data for the bright and dark tracks are similar, except that there is a shallow band minimum near 0.92–0.95 μm. (b) Transmission Mössbauer spectra (295 K) and modeled mineralogy for four of the size fractions of HWMK530 in Figure 20a. The <5-μm size fraction corresponds to the size fraction for Martian dust and npOx (brown) is the only detectable Fe-bearing phase. With increasing particle diameter, the proportion of olivine (green colored bands) increases, with 34% Fe from olivine in the 500- to 1000-μm size fraction. The sextets result from Ti-magnetite and hematite. Note that there is no detectable manifestation of the olivine in the HWMK530 Pancam-equivalent spectra.

dominated by a basaltic sand cover with a lag concentration of hematitic concretions. Areas to the south of the Opportunity site are predicted to have incorporated more dust into the ripples that dominate the plains. Plains to the south of the landing site near the contact with cratered terrain that have low albedo and low TI also have OMEGA-based spectra with a distinctive ~1-μm absorption band. We interpret these results to indicate that the surface is enhanced in fine-grained olivine for these areas, although we cannot exclude other fine-grained materials with similar features (e.g., iron oxides). Cratered terrains to the south of the plains are distinctly different from the plains and have spectral signatures dominated by pyroxenes.

[38] Results from this paper, previous work that includes the detailed work associated with the Opportunity measurements, together with mapping the nature and areal extent of hematite-bearing plains and etched terrains, provide the background for development of a model for the formation and modification of the Meridiani deposits and surfaces (Figure 21). As noted by *Hynek and Phillips* [2001], Terra Meridiani was tilted to the northwest during the Noachian Era, as the formation of the Tharsis Plateau loaded the surrounding lithosphere. They note that during or after load-induced tilting, fluvial processes generated valley systems within the cratered terrains and transported a considerable amount of material toward the northwest. In the vicinity of the Opportunity landing site, material was then deposited unconformably over the dissected cratered terrains. The areal extent of deposition covered several hundred thousand square kilometers, on the basis of the presence of partially eroded layered deposits observed beyond the landing site [*Hynek et al.*, 2002; *Arvidson et al.*, 2003; *Edgett*, 2005]. The environment of deposition for at least the uppermost part of this thick section of rock inferred from rover-based measurements of outcrops is dominated by interaction of acidic groundwater with a basaltic precursor material to produce sulfate-rich "dirty evaporite" deposits [*Squyres et al.*, 2004b; *Grotzinger et al.*, 2005]. Wind and water redistributed these materials as sands, and both aeolian and subaqueous transport are indicated by observations of current-produced sedimentary structures, including meter-scale cross bedding and centimeter-scale festoon cross lamination. After deposition, these materials also underwent substantial diagenesis as a consequence of multiple influxes of groundwater [*McLennan et al.*, 2005].

[39] The most plausible regional-scale model for formation of the Meridiani deposits is one in which the water table rose relative to the dissected cratered terrain surfaces, resulting from tectonic subsidence and/or enhanced recharge of the cratered terrain highlands to the southwest. A regime of relative uplift and dissection switched to one of relative subsidence and sedimentary accumulation onto the cratered terrains. The several kilometers of relief between the cratered highlands to the northwest and the dissected cratered terrains to the southeast would have easily produced the hydrostatic head necessary for regional-scale ground water flow. In fact, regional-scale modeling of ground water flow indicates that the Meridiani area would be one where ground water would upwell toward the surface [*Hanna and Phillips*, 2006]. Sulfur and other volatile species were introduced to the hydrologic system as a consequence of extensive volcanism from Tharsis (and

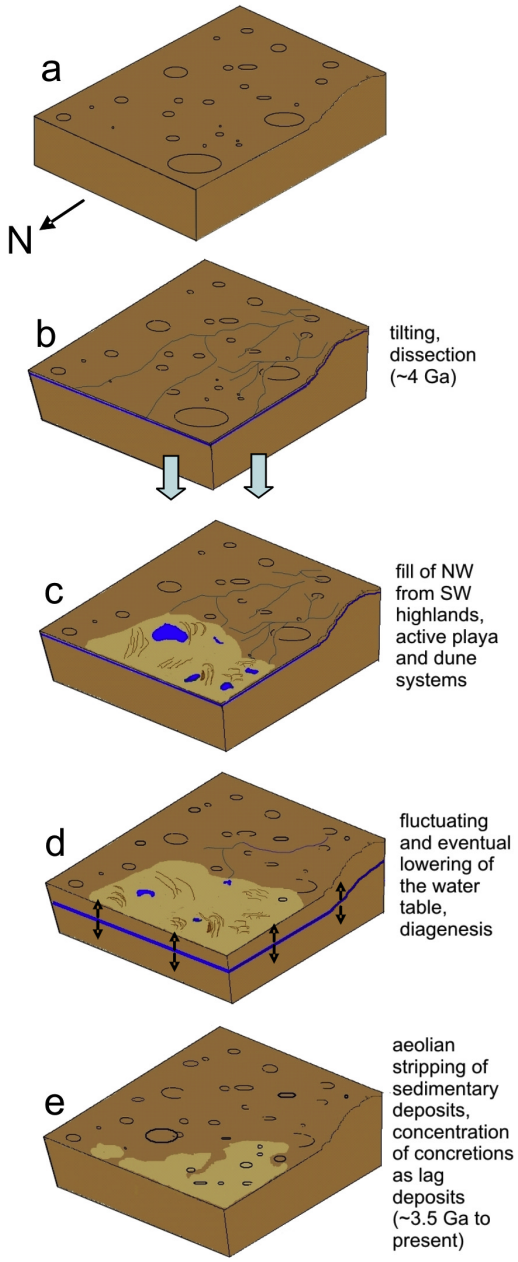

Figure 21. Schematic of Terra Meridiani regional geologic history. (a) Cratered terrain is (b) tilted to the northwest and fluvially dissected in the Noachian. (c) Debris from the southwestern highlands is transported to the northwest. Evaporation of surface waters during a period of rising water tables leads to the formation of a dune-playa system of "dirty evaporites." (d) The water table fluctuates, leading to diagenesis and concretion formation. (e) Following final lowering of the water table ~3.5 Gyr, aeolian stripping of the sedimentary deposits ensues. Hematitic concretions are concentrated as lag deposits, and a thin layer of basaltic sand is deposited.

other) volcanoes and/or by weathering of preexisting sulfur-bearing deposits and would have produced an acid-sulfate ground water system.

[40] Relative rise of the groundwater table resulted in the development of springs and playa lakes of high ionic strength within local topographic depressions. Desiccation of these local, shallow water bodies would have provided a ready source of "dirty evaporite" deposits dominated by sulfates and weathered siliciclastic components supplied as aeolian bedload or suspended dust. Evaporation of pore fluids within the capillary fringe, or surface water within playa lakes, would have precipitated evaporite minerals as cements that bound siliciclastic grains together [*Grotzinger et al.*, 2005; *McLennan et al.*, 2005]. During dry periods, erosion and redistribution of these cemented mudstones would have occurred by aeolian processes and during wetter periods by water flow. These sediments, in turn, would have accumulated across the ancient surface of Meridiani as accumulations of wind-blown sand and silt. Preservation would have been assured as the ground water table continued to rise, with associated diagenetic processes and cementation of deposits within the capillary fringe. New evaporite and related deposits would have continued to accumulate at the depositional surface as the water table continued to rise, and rose to form shallow pools that became evaporitic playas.

[41] After the Meridiani hydrologic system ceased operating aeolian processes would have taken over as the dominant process. The modern Meridiani plains formed via wind erosion of the sulfate-dominated sedimentary deposits, and accumulation of a thin veneer of aeolian basaltic sand advected into the region. Hematitic concretions formed as lag deposits as the softer sulfate rocks were eroded by wind. Occasional sulfate outcrops were exposed via cratering and in between aeolian ripples, where the basaltic sand cover is thinnest.

Appendix A

[42] THEMIS thermal inertia values were calculated using a thermal model derived from the Viking IRTM thermal model [*Kieffer et al.*, 1977, Appendix 1], with the primary modification being the replacement of a constant atmospheric thermal radiation with a one-layer atmosphere that is spectrally crystalline at solar wavelengths. The brightness temperature of the surface is determined by fitting a Planck curve to band 9 (centered at 12.57 μm) calibrated radiance after the data have been corrected for instrumental effects. Band 9 brightness temperatures are used to approximate the surface kinetic temperature, because this wavelength range is relatively transparent to atmospheric dust and has the highest signal to noise ratio. Nighttime temperature data only were used in this work because the effects of albedo and sun-heated slopes have dissipated throughout the night, and the thermal contrast due to differences in particle sizes are at a maximum [e.g., *Kieffer et al.*, 1977; *Palluconi and Kieffer*, 1981; *Christensen*, 1982]. Surface and atmospheric parameters appropriate for the THEMIS image and band 9 temperatures are then used to interpolate thermal inertia values from a seven-dimensional look-up table (season, latitude, local solar time, thermal inertia, albedo, elevation, and atmospheric dust opacity). Additional technique details, thermal inertia derivation uncertainties, and applications are provided by *Fergason et al.* [2006].

[43] The OMEGA color composite for 1183-5, MOC NA frame, and Thermal Inertia (TI) data in Figure 5 were

registered to a common base map in order to overlay the traverse of Opportunity from Eagle to Endurance craters and then south to Fruitbasket. The base map was created from four THEMIS visible images that were projected into a sinusoidal projection and compiled into an uncontrolled mosaic. A series of match points were selected on the OMEGA and TI images, and the corresponding points were identified in the base map. The match point data were used to transform the OMEGA and TI images into the same projection as the base map. A MOC NA image (frame R14000021) with an overlay of the Opportunity traverse was registered to the base map in a similar manner so that the traverse could be transferred to the OMEGA and TI images. The MOC NA image in Figure 5 was not registered to the base map, because it was much higher resolution. Instead, the MOC image was map projected into an equirectangular projection with pixel spacing of 2 m.

[44] **Acknowledgments.** We thank the superb group of engineers and payload personnel who have made the Opportunity and OMEGA observations, and we thank NASA for support of Athena Science Team Members.

References

Adams, J. (1975), Interpretation of visible and near-infrared diffuse reflectance spectra of pyroxenes and other rock-forming minerals, in *Infrared and Raman Spectroscopy of Lunar and Terrestrial Minerals*, edited by C. Karr Jr., pp. 91–116, Elsevier, New York.

Albee, A. L., R. E. Arvidson, F. Palluconi, and T. Thorpe (2001), Overview of the Mars Global Surveyor mission, *J. Geophys. Res.*, *106*(E10), 23,291–23,316.

Arvidson, R. E., F. Seelos IV, K. Deal, W. Koeppen, N. Snider, J. Kieniewicz, B. Hynek, M. Mellon, and J. Garvin (2003), Mantled and exhumed terrains in Terra Meridiani, Mars, *J. Geophys. Res.*, *108*(E12), 8073, doi:10.1029/2002JE001982.

Arvidson, R. E., et al. (2004), Localization and physical properties experiments conducted by Opportunity at Meridiani Planum, *Science*, *306*(5702), 1730–1733, doi:10.1126/science.1104211.

Arvidson, R. E., F. Poulet, J.-P. Bibring, M. Wolff, A. Gendrin, R. V. Morris, J. J. Freeman, Y. Langevin, N. Mangold, and G. Bellucci (2005), Spectral reflectance and morphologic correlations in eastern Terra Meridiani, Mars, *Science*, *307*(5715), 1591–1594, doi:10.1126/science.1109509.

Arvidson, R. E., et al. (2006), Overview of the Spirit Mars Exploration rover mission to Gusev crater: Landing site to Backstay rock in the Columbia Hills, *J. Geophys. Res.*, *111*, E02S01, doi:10.1029/2005JE002499.

Bandfield, J. L. (2002), Global mineral distributions on Mars, *J. Geophys. Res.*, *107*(E6), 5042, doi:10.1029/2001JE001510.

Bandfield, J. L., V. E. Hamilton, and P. R. Christensen (2000), A global view of Martian surface compositions from MGS-TES, *Science*, *287*, 1626–1630.

Bell, J. F., R. V. Morris, and J. B. Adams (1993), Thermally altered palagonitic tephra: A spectral and process analog to the soil and dust of Mars, *J. Geophys. Res.*, *98*(E2), 3373–3385.

Bell, J. F., III, et al. (2003), Mars Exploration rover Athena Panoramic Camera (Pancam) investigation, *J. Geophys. Res.*, *108*(E12), 8063, doi:10.1029/2003JE002070.

Bell, J. F., III, et al. (2004), Pancam multispectral imaging results from the Opportunity rover at Meridiani Planum, *Science*, *306*(5702), 1703–1709, doi:10.1126/science.1105245.

Bibring, J.-P., et al. (2005), Mars surface diversity as revealed by the OMEGA/Mars Express observations, *Science*, *307*(5715), 1576–1581, doi:10.1126/science.1109509.

Chapman, C. R., and K. L. Jones (1977), Cratering and obliteration history of Mars, *Annu. Rev. Earth Planet. Sci.*, *5*, 515–540.

Christensen, P. R. (1982), Martian dust mantling and surface composition: Interpretation of thermophysical properties, *J. Geophys. Res.*, *87*(B12), 9985–9998.

Christensen, P. R., and S. W. Ruff (2004), Formation of the hematite-bearing unit in Meridiani Planum: Evidence for deposition in standing water, *J. Geophys. Res.*, *109*, E08003, doi:10.1029/2003JE002233.

Christensen, P. R., et al. (2000), Detection of crystalline hematite mineralization on Mars by the Thermal Emission Spectrometer: Evidence for near-surface water, *J. Geophys. Res.*, *105*(E4), 9623–9642.

Christensen, P. R., R. V. Morris, M. D. Lane, J. L. Bandfield, and M. C. Malin (2001), Global mapping of Martian hematite deposits: Remnants of water-driven processes on early Mars, *J. Geophys. Res.*, *106*(E10), 23,873–23,886.

Christensen, P. R., et al. (2003), Miniature Thermal Emission Spectrometer for the Mars Exploration rovers, *J. Geophys. Res.*, *108*(E12), 8064, doi:10.1029/2003JE002117.

Christensen, P. R., et al. (2004a), The Thermal Emission Imaging System (THEMIS) for the Mars 2001 Odyssey mission, *Space Sci. Rev.*, *110*, 85–130.

Christensen, P. R., et al. (2004b), Mineralogy at Meridiani Planum from the Mini-TES experiment on the Opportunity rover, *Science*, *306*(5702), 1733–1739, doi:10.1126/science.1104909.

Clancy, R. T., M. J. Wolff, and P. R. Christensen (2003), Mars aerosol studies with the MGS TES emission phase function observations: Optical depths, particle sizes, and ice cloud types versus latitude and solar longitude, *J. Geophys. Res.*, *108*(E9), 5098, doi:10.1029/2003JE002058.

Edgett, K. S. (2005), The sedimentary rocks of Sinus Meridiani: Five key observations from data acquired by the Mars Global Surveyor and Mars Odyssey orbiters, *Mars*, *1*, 5–58, doi:10.1555/mars.2005.0002.

Erard, S., and W. Calvin (1997), New composite spectra of Mars, 0.4–5.7 μm, *Icarus*, *130*(2), 449–460, doi:10.1006/icar.1997.5830.

Fergason, R. L., P. R. Christensen, and H. H. Kieffer (2006), High-resolution thermal inertia derived from THEMIS: Thermal model and applications, *J. Geophys. Res.*, doi:10.1029/2006JE002735, in press.

Gendrin, A., et al. (2005), Sulfates in Martian layered terrains: The OMEGA/Mars Express view, *Science*, *307*(5715), 1587–1591, doi:10.1126/science.1109509.

Grotzinger, J. P., et al. (2005), Stratigraphy and sedimentology of a dry to wet eolian depositional system, Burns formation, Meridiani Planum, Mars, *Earth Planet. Sci. Lett.*, *240*(1), 11–72, doi:10.1016/j.epsl.2005.09.039.

Hamilton, V. E., M. B. Wyatt, H. Y. McSween Jr., and P. R. Christensen (2001), Analysis of terrestrial and Martian volcanic compositions using thermal emission spectroscopy: 2. Application to Martian surface spectra from the Mars Global Surveyor Thermal Emission Spectrometer, *J. Geophys. Res.*, *106*(E7), 14,733–14,746.

Hanna, J. C., and R. J. Phillips (2006), Tharsis-driven hydrology and the Martian outflow channels, *Lunar Planet. Sci.*, *XXXVII*, abstract 2373.

Hartmann, W. K., and G. Neukum (2001), Cratering chronology and the evolution of Mars, *Space Sci. Rev.*, *96*, 165–194.

Herkenhoff, K. E., et al. (2003), Athena Microscopic Imager investigation, *J. Geophys. Res.*, *108*(E12), 8065, doi:10.1029/2003JE002076.

Herzberg, G. (1945), *Molecular Spectra and Molecular Structure*, vol. 2, *Infrared and Raman Spectra of Polyatomic Molecules*, Van Nostrand Reinhold, Hoboken, N. J.

Hynek, B. M., and R. J. Phillips (2001), Evidence for extensive denudation of the Martian highlands, *Geology*, *29*, 407–410.

Hynek, B. M., R. E. Arvidson, and R. J. Phillips (2002), Geologic setting and origin of Terra Meridiani hematite deposit on Mars, *J. Geophys. Res.*, *107*(E10), 5088, doi:10.1029/2002JE001891.

Jerolmack, D. J., D. Mohrig, J. P. Grotzinger, D. A. Fike, and W. A. Watters (2005), Spatial grain-size sorting in eolian ripples and estimation of wind conditions on planetary surfaces: Application to Meridiani Planum, Mars, *J. Geophys. Res.*, *111*, E12S02, doi:10.1029/2005JE002544.

Jouglet, D., F. Poulet, J. F. Mustard, R. E. Milliken, J. P. Bibring, Y. Langevin, and B. Gondet (2006), Observation of 3 μm hydration feature on Mars from OMEGA-MEx data, *Lunar Planet Sci.*, *XXXVII*, abstract 1741.

Kieffer, H. H., T. Z. Martin, A. R. Peterfreund, and B. M. Jakosky (1977), Thermal and albedo mapping of Mars during the Viking primary mission, *J. Geophys. Res.*, *82*(28), 4249–4291.

Klingelhöfer, G., et al. (2003), Athena MIMOS II Mössbauer spectrometer investigation, *J. Geophys. Res.*, *108*(E12), 8067, doi:10.1029/2003JE002138.

Klingelhöfer, G., et al. (2004), Jarosite and hematite at Meridiani Planum from Opportunity's Mossbauer spectrometer, *Science*, *306*(5702), 1740–1745, doi:10.1126/science.1104653.

Lane, M. D., R. V. Morris, S. A. Mertzman, and P. R. Christensen (2002), Evidence for platy hematite grains in Sinus Meridiani, Mars, *J. Geophys. Res.*, *107*(E12), 5126, doi:10.1029/2001JE001832.

Maki, J. N., et al. (2003), Mars Exploration rover engineering cameras, *J. Geophys. Res.*, *108*(E12), 8071, doi:10.1029/2003JE002077.

Malin, M. C., G. E. Danielson, A. P. Ingersoll, H. Masursky, J. Veverka, M. A. Ravine, and T. A. Soulanille (1992), Mars Observer Camera, *J. Geophys. Res.*, *97*(E5), 7699–7718.

McLennan, S. M., et al. (2005), Provenance and diagenesis of the evaporite-bearing Burns formation, Meridiani Planum, Mars, *Earth Planet. Sci. Lett.*, *240*(1), 95–121, doi:10.1016/j.epsl.2005.09.041.

Morris, R. V., et al. (2000), Mineralogy, composition, and alteration of Mars Pathfinder rocks and soils: Evidence from multispectral, elemental, and

magnetic data on terrestrial analogue, SNC meteorite, and Pathfinder samples, *J. Geophys. Res.*, *105*(E1), 1757–1817.
Morris, R. V., et al. (2006), Mössbauer mineralogy of rock, soil, and dust at Meridiani Planum, Mars: Opportunity's journey across sulfate-rich outcrop, basaltic sand and dust, and hematite lag deposits, *J. Geophys. Res.*, *111*, E02S13, doi:10.1029/2005JE002584.
Neukum, G., and B. A. Ivanov (1996), The size-frequency distribution of impact craters in the inner solar system and implications for past and recent cratering rates in the Earth-Moon system, *Meteor. Planet. Sci.*, *31*, A97.
Palluconi, F. D., and H. H. Kieffer (1981), Thermal inertia mapping of Mars from 60°S to 60°N, *Icarus*, *45*, 415–426.
Pieters, C. M., E. M. Fischer, O. Rode, and A. Basu (1993), Optical effects of space weathering: The role of the finest fraction, *J. Geophys. Res.*, *98*(E11), 20,817–20,824.
Poulet, F., and S. Erard (2004), Nonlinear spectral mixing: Quantitative analysis of laboratory mineral mixtures, *J. Geophys. Res.*, *109*, E02009, doi:10.1029/2003JE002179.
Poulet, F., J. N. Cuzzi, D. P. Cruikshank, T. Roush, and C. M. Dalle Ore (2002), Comparison between the Shkuratov and Hapke scattering theories for solid planetary surfaces: Application to the surface composition of two Centaurs, *Icarus*, *160*, 313–324.
Poulet, F., J.-P. Bibring, J. F. Mustard, A. Gendrin, N. Mangold, Y. Langevin, R. E. Arvidson, B. Gondet, and C. Gomez (2005), Phyllosilicates on Mars and implications for early Martian climate, *Nature*, *438*(7068), 623–627, doi:10.1038/nature04274.
Presley, M. A., and P. R. Christensen (1997), Thermal conductivity measurements of particulate materials: 2. Results, *J. Geophys. Res.*, *102*(E3), 6551–6566.
Rieder, R., R. Gellert, J. Brückner, G. Klingelhöfer, G. Dreibus, A. Yen, and S. Squyres (2003), The new Athena alpha particle X-ray spectrometer for the Mars Exploration rovers, *J. Geophys. Res.*, *108*(E12), 8066, doi:10.1029/2003JE002150.
Saunders, R. S., et al. (2004), 2001 Mars Odyssey mission summary, *Space Sci. Rev.*, *110*, 1–36.
Shkuratov, Y., L. Starukhina, H. Hoffmann, and G. Arnold (1999), A model of spectral albedo of particulate surfaces: Implications for optical properties of the Moon, *Icarus*, *137*, 235–246.
Singer, R. B. (1981), Near-infrared spectral reflectance of mineral mixtures: Systematic combinations of pyroxenes, olivine, and iron oxides, *J. Geophys. Res.*, *86*(B9), 7967–7982.
Smith, M. D. (2004), Interannual variability in TES atmospheric observations of Mars during 1999–2003, *Icarus*, *167*, 148–165.
Smith, M. D., et al. (2004), First atmospheric science results from the Mars Exploration rovers Mini-TES, *Science*, *306*, 1750–1753.
Soderblom, L. A., et al. (2004), Soils of Eagle crater and Meridiani Planum at the Opportunity rover landing site, *Science*, *306*(5702), 1723–1726, doi:10.1126/science.1105127.
Squyres, S. W., et al. (2003), The Athena Mars rover science investigation, *J. Geophys. Res.*, *108*(E12), 8062, doi:10.1029/2003JE002121.
Squyres, S. W., et al. (2004a), The Opportunity rover's Athena science investigation at Meridiani Planum, Mars, *Science*, *306*(5702), 1698–1703, doi:10.1126/science.1106171.
Squyres, S. W., et al. (2004b), In situ evidence for an ancient aqueous environment at Meridiani Planum, *Mars, Science*, *306*(5702), 1709–1714, doi:10.1126/science.1104559.
Stamnes, K., S. Tsay, W. Wiscombe, and K. Jayaweera (1988), Numerically stable algorithm for discrete-ordinate-method radiative transfer in multiple scattering and emitting layered media, *Appl. Opt.*, *27*, 2502–2509.
Sullivan, R., et al. (2005), Aeolian processes at the Mars Exploration rover Meridiani Planum landing site, *Nature*, *436*, 58–61.
Weitz, C. M., R. C. Anderson, J. F. Bell III, W. H. Farrand, K. E. Herkenhoff, J. R. Johnson, B. L. Jolliff, R. V. Morris, S. W. Squyres, and R. J. Sullivan (2006), Soil grain analyses at Meridiani Planum, Mars, *J. Geophys. Res.*, *111*, E12S04, doi:10.1029/2005JE002541.
Wolff, M. J., and R. T. Clancy (2003), Constraints on the size of Martian aerosols from TES spectral observations, *J. Geophys. Res.*, *108*(E9), 5097, doi:10.1029/2003JE002057.

R. E. Arvidson, J. L. Griffes, E. A. Guinness, K. Seelos, J. G. Ward, and S. M. Wiseman, Department of Earth and Planetary Sciences, Washington University, Campus Box 1167, One Brookings Drive, St. Louis, MO 63130, USA. (arvidson@wunder.wustl.edu)
J. F. Bell III, S. W. Squyres, and R. J. Sullivan, Dept. of Astronomy, Cornell University, Ithaca, NY 14853, USA.
G. Bellucci, Istituto di Fisica dello Spazio Interplanetario, INAF, I-00133, Rome, Italy.
J.-P. Bibring, B. Gondet, Y. Langevin, and F. Poulet, Institut d'Astrophysique Spatiale, Université Paris-Sud, Orsay, F-91405, France.
P. R. Christensen and R. L. Fergason, Department of Geological Sciences, Arizona State University, Tempe, AZ 85287, USA.
B. L. Ehlmann, School of Geography and Environment, University of Oxford, OX1 3QY, UK.
W. H. Farrand and M. Wolff, Space Science Institute, Boulder, CO 80301, USA.
M. Golombek, Jet Propulsion Laboratory, Pasadena, CA 91109, USA.
J. Grotzinger, Geological and Planetary Sciences, California Institute of Technology, Pasadena, CA 91125, USA.
K. E. Herkenhoff and J. R. Johnson, U.S. Geological Survey, Flagstaff, AZ 86001, USA.
G. Klingelhöfer, Institut für Anorganische und Analytische Chemie, Johannes Gutenberg-Universität, D-55128 Mainz, Germany.
D. Ming and R. V. Morris, NASA Johnson Space Center, Houston, TX 77058, USA.